Evaluation of the Tactoid Formation in Clay Systems

Jansson, Maria

2019

Document Version:
Publisher's PDF, also known as Version of record

Evaluation of the Tactoid Formation in Clay Systems

MARIA JANSSON | DIVISION OF THEORETICAL CHEMISTRY | LUND UNIVERSITY

Evaluation of the Tactoid Formation in Clay Systems

Maria Jansson

Division of Theoretical Chemistry
Lund University, Sweden

LUND
UNIVERSITY

Licentiate Thesis

Faculty opponent:
Professor emeritus Staffan Hansen,
Centre for Analysis and Synthesis
Department of Chemistry
Faculty of Engineering, Lund University

To be presented, with the permission of the Faculty of Science, Lund University, for public criticism in lecture hall A, Center for Chemistry and Chemical Engineering, Lund, Friday May 3 2019, 10:15.

Organization
LUND UNIVERSITY

Division of Theoretical Chemistry
P. O. Box 124
SE–221 00 LUND
Sweden

Author(s)
Maria Jansson

Document name
LICENTIATE THESIS

Date of disputation
2019-05-03

Sponsoring organization
eSSENCE, the Swedish national strategic e-science research program.

Title and subtitle
Evaluation of the Tactoid Formation in Clay Systems

Abstract
Clay minerals consist of anisotropic nanoplatelets where the majority of the clay minerals are highly charged, and thus, swell in aqueous solution. The structure and swelling depend on the type of clay mineral, and also on the ionic composition, and temperature. The natural clay mineral montmorillonite have been studied both theoretically and experimentally. Theoretically, coarse-grained models have been used to represent the clay platelets where Monte Carlo (MC), and molecular dynamics (MD) simulations have been utilized to study the electrostatic interactions between the platelets. Experimentally, the structure has been studied with small angle X-ray scattering (SAXS), and the swelling has been studied by swelling pressure measurements in a test cell.

The research in this thesis has been focused on the tactoid formation, i.e. platelets aggregating in a face-to-face configuration with an equidistant separation, as a function of the divalent counterion charge ratio, and as an effect of the relative permittivity of the solvent. It was found that it was possible to tune the electrostatic interactions to obtain a transition from a repulsive to an attractive system when increasing the divalent counterion charge ratio or by decreasing the relative permittivity of the solvent. Moreover, the temperature response was investigated, where it was found that the electrostatic interactions alone can give a positive, negative, or constant osmotic pressure response with temperature.

Key words
Clay, Montmorillonite, Nanoplatelets, Tactoid, Anisotropy, Coarse-grained models, MD simulations, MC simulations, SAXS, Swelling pressure

Classification system and/or index terms (if any)

Supplementary bibliographical information

Language
English

ISSN and key title

ISBN
978-91-7422-648-5 (print)
978-91-7422-649-2 (pdf)

Recipient's notes

Number of pages
72

Price

Security classification

Evaluation of the Tactoid Formation in Clay Systems

Maria Jansson

LUND
UNIVERSITY

Licentiate Thesis
2019

EVALUATION OF THE TACTOID FORMATION IN CLAY SYSTEMS

Front cover:
Image from Pixabay

Back cover:
Montmorillonite from Cortijo de Archidona Clay Mine, Cabo de Gata, Almería, Spain.
Photo by Maria Jansson

Theoretical Chemistry
Department of Chemistry
Faculty of Science
Lund University

ISBN: 978-91-7422-648-5 (print)
ISBN: 978-91-7422-649-2 (pdf)

Printed in Sweden by Media-Tryck, Lund University, Lund 2019

Media-Tryck is an environmentally certified and ISO 14001:2015 certified provider of printed material. Read more about our environmental work at www.mediatryck.lu.se

MADE IN SWEDEN

Abstract

Clay minerals consist of anisotropic nanoplatelets where the majority of the clay minerals are highly charged, and thus, swell in aqueous solution. The structure and swelling depend on the type of clay mineral, and also on the ionic composition, and temperature. The natural clay mineral montmorillonite have been studied both theoretically and experimentally. Theoretically, coarse-grained models have been used to represent the clay platelets where Monte Carlo (MC), and molecular dynamics (MD) simulations have been utilized to study the electrostatic interactions between the platelets. Experimentally, the structure has been studied with small angle X-ray scattering (SAXS), and the swelling has been studied by swelling pressure measurements in a test cell.

The research in this thesis has been focused on the tactoid formation, i.e. platelets aggregating in a face-to-face configuration with an equidistant separation, as a function of the divalent counterion charge ratio, and as an effect of the relative permittivity of the solvent. It was found that it was possible to tune the electrostatic interactions to obtain a transition from a repulsive to an attractive system when increasing the divalent counterion charge ratio or by decreasing the relative permittivity of the solvent. Moreover, the temperature response was investigated, where it was found that the electrostatic interactions alone can give a positive, negative, or constant osmotic pressure response with temperature.

Contents

List of publications

This thesis is based on the following publications, referred to by their Roman numerals:

I **Temperature Response of Charged Colloidal Particles by Mixing Counterions Utilizing Ca^{2+}/Na^{+} Montmorillonite as Model System**

A. Thuresson, **M. Jansson**, T. S. Plivelic and M. Skepö
Journal of Physical Chemistry C, 2017, 121, pp. 7951–7958

II **The Effect of the Relative Permittivity on the Tactoid Formation in Nanoplatelet Systems. A Combined Computer Simulation, SAXS, and Osmotic Pressure Study**

M. Jansson, A. Thuresson, T. S. Plivelic, J. Forsman and M. Skepö
Journal of Colloid and Interface Science, 2018, 513, pp. 575–584

Populärvetenskaplig sammanfattning

Lera består utav små finkorninga lermineraler, vilka utgörs till stor del av elektrostatiskt laddade nanopartiklar, även kallade lerplattor. En lerplatta har en tjocklek på en miljarddels meter och dess diameter kan variera alltifrån fem till tusen gånger större än tjockleken, vilket kan jämföras med ett A4-ark, där kortsidan är tusen gånger större än tjockleken. Denna storleksskillnad ger upphov till att lerplattorna är anisotropa, alltså att de har olika fysikaliska egenskaper i olika riktningar. Vad gäller lermineralens specifika struktur, egenskaper och komposition finns det en stor variation där ingen är den andra lik och detta beror på vilken typ av bergart lermineralen kommer ifrån. I huvudsak består en lerplatta utav ett tetraediskt lager innehållandes kisel som är omgivet av varsitt oktaedriskt lager innehållandes aluminium på båda sidor. Denna struktur är negativ laddad då det förekommer utbyten mellan kisel och aluminium jonerna mot joner med lägre laddning (valens), och för att bibehålla ett neutralt system existerar det positiva joner (motjoner) mellan lerplattorna. Det är denna negativa laddning på lerplattorna och dess motjoner som ger upphov till lerans svällande egenskaper.

Lera används inom många tillämpningsområden, bland annat vid kärnavfallsförvaring, papperstillverkning och vid borrning av gas eller olja. För slutförvaringen av det farliga radioaktiva avfallet från de svenska kärnkraftverken planerar Sverige att placera avfallet i kopparkapslar som skall bäddas in i bentonitlera 500 meter under marken i urberget. Bentonitleran består till huvudsak av lermineralen montmorillonit, och tanken är att denna skall skydda kopparkapseln både fysiskt och kemiskt under väldigt lång tid. På grund utav detta är det mycket viktigt att utvärdera lerans egenskaper samt hur den påverkas av exempelvis jonerna i grundvattnet, temperatur och tryck, allt för att få en förståelse över hur den beter sig under olika faktorer.

I studierna som är presenterade i denna uppsats har lermineralen montmorillonit använts för att undersöka hur dess strukturella egenskaper och svällning beror på andelen divalenta motjoner, temperatur och typ av lösningsmedel, vilka har studerats både te-

oretiskt med datorsimuleringar samt med olika experimentella tekniker. Exempelvis, strukturen har analyserat med ljusspridning och det osmotiska trycket har mätts med hjälp av tryckmätningar i en test cell. Teoretiskt, har grovkorninga modeller använts för att representera lerplattorna, antingen som två laddade parallella oändliga ytor eller som flera små laddade plattor i en låda. Syftet med simuleringarna är att försöka få en koppling mellan teori och experimentella observationer. Främst har fokus legat på att få en förståelse över hur de elektrostatiska interaktionerna inom systemet påverkar dess struktur och svällning.

Det har visats sig att det är möjligt hitta en övergång ifrån ett repulsivt till ett attraktivt system enbart genom att justera de elektrostatiska interaktionerna i systemet. Detta fångades genom att antingen ändra valensen på motjonerna, från monovalent till divalent, eller genom att ändra lösningsmedlet, från vatten till alkohol. Dessutom, visade det sig att temperaturen har en påverkan på systemet, där det osmotiska trycket antingen kunde vara positivt, negativt eller konstant beroende på temperatur och typ av motjon, vilket kan beskrivas enbart utifrån de elektrostatiska interaktionerna.

1. Introduction

1.1 Clay and clay minerals

Clay science is a broad interdisciplinary field dating back to the mid-1930s (Bergaya et al. (2006)), and prior to the development of modern analytical techniques it was difficult to characterize small-sized particles composed of crystal imperfections in various degrees. This adversity led quite naturally to problems with the nomenclature of the terms clay and clay mineral. However, the development and improvements of different analytical techniques in the 1950s made it possible to accumulate information about the identification of clay. Since then, clay scientists have made attempts to unify the nomenclature and classification of clay on an international level (Bailey (1980)). One of the definitions of clay is: a naturally occuring material composed of primarily fine-grained minerals, which is generally plastic at appropriate water contents, and will harden when dried or fired. In the classification, the fine-grained minerals are defined to have an upper size limit of about 2-4 μm. Furthermore, clay minerals can be defined as: phyllosilicateminerals and minerals which impart plasticity to clay and hardens upon drying or firing (Guggenheim & Martin (1995)).

Clay minerals are formed in soils, sediments and by diagenetic alteration of volcanic ash, and depending on which type of rock it is originated from, there is a wide variation of clay minerals with different compositions, structures, and properties. These clay minerals belong to the family of phyllosilicates, or layer silicates, and the majority are aluminosilicates. The structural layers consist of two-dimensional continous (Si,Al)-O tetrahedral (T) sheets, which are linked in the unit structure to (Al,Mg,Fe)-O octahedral (O) sheets, or to groups of coordinated cations, or individual cations (Bailey (1980); Deer et al. (2013)). The structure of the octahedral component is either defined as di- or trioctahedral, depending on whether there are two or three trivalent cations in the O sheet. Moreover, the T and O sheets can be connected in T-O pairs or in T-O-T groups, thus, clay minerals are divided into two main types, 1:1 (TO), and 2:1 (TOT) layer clay minerals, which is schematically illustrated in Fig. 1.1. The primary

groups of clay minerals are: (i) kaolinite, (ii) illite, (iii) smectite, and (iv) vermiculite. Kaolinites are dioctahedral and belongs to the 1:1 clay minerals, where the thickness of the single silica T sheet and the single alumina O sheet is about 0.7 nm (Fig. 1.1a). The ideal chemical formula of kaolinite is $Al_2[Si_2O_5](OH)_4$, and it is a non-swelling clay mineral due to the strong attraction between the adjacent layers, i.e. hydrogen bonding between the OH groups of the O sheet and oxygens of the T sheet (Grim (1953); Bergaya et al. (2006); Deer et al. (2013)).

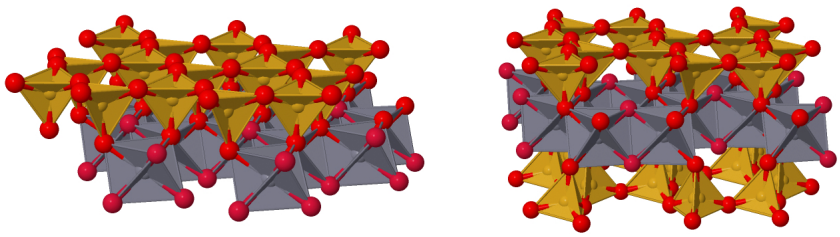

(a) (b)

Figure 1.1: Schematically illustrated structures of (a) a 1:1 (TO), and (b) a 2:1 (TOT) clay mineral. The tetrahedral silica sheet is represented in beige, the octahedral alumina sheet is represented in grey, and the connecting oxygen atoms are represented by the red spheres.

The groups of illite, smectite, and vermiculite all belongs to the 2:1 clay minerals. The structural layer consists of one central O sheet sandwiched between two T sheets with a thickness of about 1 nm, and is denoted as a clay *platelet* (Fig. 1.1b). The octahedral component for the clay minerals within the groups differs, for illites it is mostly dioctahedral, for vermiculites it is mostly trioctahedral, and for smectites it can be either di- or trioctahedral depending on the smectite. The main smectites are montmorillonite, beidellite, nontronite, saponite, hectorite, and suconite, where the three former have a dioctahedral structure, and the three latter are trioctahedral. The characteristic feature of a 2:1 clay mineral is the permanent negative surface charge density, which originates from either (i) substitution of Si^{4+} ions by Al^{3+} ions in the tetrahedral sheet, (ii) substitution of Al^{3+} ions or Mg^{2+} ions by cations with a lower valency in the octahedral sheet, or (iii) vacancies. To conserve electroneutrality, the net-charge deficiency is balanced by charge compensating exchangeable cations adsorbed in the interlayer between the platelets (Grim (1953); Deer et al. (2013)). Moreover, the sign and density of the clay platelets edge charges depends on the pH of the dispersion, which arises from that the 'broken bonds' of Si-O-Si and Al-O-Al, converts into hydroxyl groups of Si-OH and Al-OH, thus, the edges can have either positive, negative or neutral charges (Bergaya et al. (2006)).

The structural and charge anisotropy of the clay platelets gives rise to the specific structural and dynamic properties. Several configurations of the clay platelets in a clay

have been proposed, such as (i) *House-of-Cards*, where the adjacent platelets are in a T configuration, (ii) *Stacked Platelets*, in which the platelets aggregate in a face-to-face configuration with an equidistant separation, denoted as tactoid (Fig. 1.2a), and (iii) *Overlapping Coins*, where the configuration consists of a band-like structure (Fig. 1.2b) (Delhorme et al. (2012)).

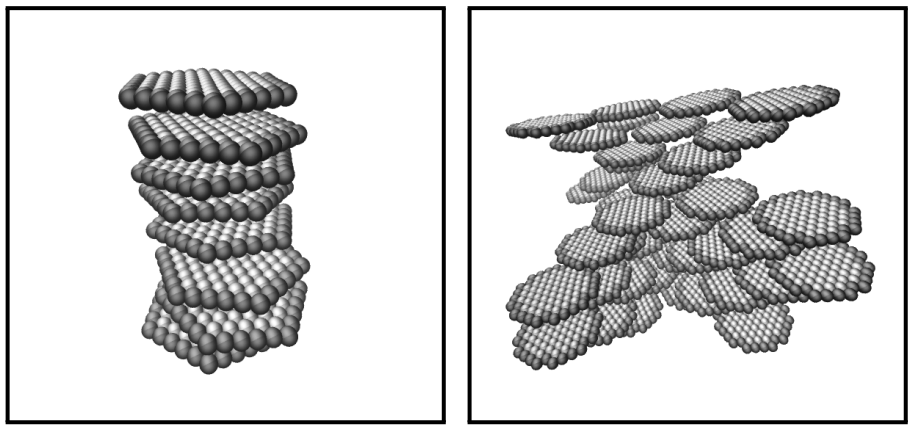

(a) (b)

Figure 1.2: Illustrative representations for the configuration of (a) stacked platelets, i.e. tactoid, and (b) overlapping coins. The platelets have a negative surface charge and a positive edge charge, where the negatively, and positively charged sites are represented as light and dark gray spheres, respectively.

1.2 Montmorillonite

The smectite montmorillonite consists of polydisperse clay platelets in the lateral dimensions, where the diameter are typically found in the range $\sim$ 5-1000 nm (Michot et al. (2004)). The ideal chemical formula (Karnland et al. (2006); Deer et al. (2013)) is defined as:

$$\mathrm{M_{x+y}(Si_{8-}{}_{x}Al_{x})(Al_{4-}{}_{y}Mg_{y}(Fe))O_{20}(OH)_{4}} \cdot n\mathrm{H_{20}}\,. \tag{1.1}$$

Here M represents the monovalent positively charged counterions located in the interlayer between the platelets, x is the amount of substituted Si^{4+} ions by Al^{3+} ions in the T sheet, and y is the amount of substituted Al^{3+} ions by Mg^{2+} ions in the O sheet. Depending on the substitution parameters x and y, the surface charge density for montmorillonite varies in the range of 0.4 to 1.2 unit charges per $O_{20}(OH)_4$-unit, i.e. $0.4 < (x + y) < 1.2$, and by definition the charge of the T sheet is lower than the O sheet, i.e. $x < y$ (Karnland et al. (2006); Hedström et al. (2011)). The negative surface

charge is neutralized by ($x + y$) monovalent counterions such as Na^+, K^+, and/or Li^+ ions. However, the cation exchange capacity (CEC) of montmorillonite makes it possible to exchange the valency of the counterions by replacing the monovalent ions with multivalent ions, such as Ca^{2+}, Mg^{2+}, and/or La^{3+} ions. The structural and swelling properties of montmorillonite are strongly affected by the valency and type of the counterion. For the monovalent ions Na^+ and Li^+, the clay platelets can dissociate and swell extensively, while for multivalent counterions tactoids are formed with an equidistant separation of about 2 nm (Bergaya et al. (2006); Segad et al. (2015)).

A high content of the montmorillonite clay mineral can be found in the natural bentonite clay MX-80, which is a Wyoming bentonite produced by the Amercian Colloid Company. MX-80 contains about 80% of montmorillonite, and the counterions are usually a mixture of both mono-, and divalent cations, where Na^+ is the dominating counterion. The bentonite clay is often described through its dominating counterion, since it, to a large extent determines the swelling property in water. Thus, MX-80 is referred as sodium bentonite or sodium saturated montmorillonite from MX-80 with the chemical formula (Karnland et al. (2006)):

$$Na_{0.65}(Si_{7.89}Al_{0.11})(Al_{3.10}Mg_{0.49}Fe_{0.38}Ti_{0.01})O_{20}(OH)_4\,. \tag{1.2}$$

Bentonite clay is planned to be used as a barrier material in repositories for final storage of highly radioactive spent nuclear fuel, where MX-80 is a suggested candiate. The clay will act as an sealing buffer and should fulfill the following properties: (i) high swelling capacity in order to seal itself around the canister and fill any cracks in the bedrock, (ii) low hydraulic conductivity to minimize any mass transport to and from the canister in order to protect it from corrosion and, in case a canister breaks, prevent any radioactive substances to leak into the bedrock, (iii) appropiate plasticity and stiffness to retain the canister in its position and reduce the force from any movements of the bedrock, (iv) long-term stability, since the time period for the radioactive material to become harmless to humans can be up to one million years, and (v) high thermal conductivity to ensure rapid transfer of the heat generated by the decay of the radioactive material (Karnland et al. (2006); SKB (2011)).

2. Fundamental theory

2.1 Statistical mechanics and thermodynamics

Statistical mechanics aims to provide a molecular interpretation of equilibrium properties for macroscopic systems, where the approach is to derive the systems thermodynamic properties from the statistical average of the systems microscopic properties. Some of the thermodynamic properties are energy, volume, particle number, pressure, temperature, and density, where the three former are extensive properties, and the three latter are intensive properties. This section is intented to provide information for some of the key concepts of statistical mechanics and thermodynamics, and for a more detailed and in-depth description, the following references are recommended: Callen (1985); Hill (1986).

2.2 Statistical thermodynamics

The part of statistical mechanics where the thermodynamic behaviour of large systems is explained by extending the classical thermodynamics is known as equilibrium statistical mechanics or statistical thermodynamics.

In a classical system, all the possible states are represented in the *phase space*. Thus, for a system with N particles, the phase space is a 6N-dimensional space where each state is represented by a vector describing the position (x, y, z), and the momenta (p_x, p_y, p_z), of all N particles. After a long time, when all of the phase space have been explored, and there is no macroscopic flow of energy or matter, the system has reached *thermodynamic equilibrium*. This refers to the first postulate of statistical mechanics: *the (long) time average of a mechanical variable in the thermodynamic system of interest is equal to the ensemble average* (the concept of an ensemble is explained in Section 2.3). Hence, a certain property is expected to have a constant value at equilibrium if it is measured over a long time.

2.3 Thermodynamic ensembles

A central concept in statistical mechanics is the *thermodynamic ensemble*, which is an imaginary collection of a very large number of systems, representing the set of all possible states of a system at equilibrium, where the average value measured over a long time is equal to the *ensemble average*, according to the *ergodic hypothesis*. The systems within an ensemble are equal at a thermodynamic level and differs at the microscopic level, thus, the ensembles are classified according to the representative macroscopic system.

The *microcanonical* ensemble represents the set of all possible states of an *isolated* system. An isolated system is a completely disconnected system where there is no transport of energy or matter in or out of the system, i.e. the number of particles (N), volume (V), and total energy (U) are constant. Thus, the second postulate of statistical mechanics is valid for the microcanonical ensemble, which states that: *for an ensemble representative of an isolated thermodynamic system, the systems of the ensemble are distributed uniformly with equal probability over the possible quantum states consistent with the specified values N, V, U*. This is also known as the principle of equal a *priori* probabilities, i.e. all microscopic states consistent with the microcanonical constraints is equally probable. The entropy (S) of the microcanonical ensemble is given by:

$$S = k_B \ln \Omega_{N,V,U} \, . \tag{2.1}$$

k_B is the Boltzmann constant, and $\Omega_{N,V,U}$ is the *microcanonical partition function* corresponding to the possible states for a constant number of particles, volume, and total energy. The maximum of the entropy is found at equilibrium, and the systems thermodynamic properties, such as the temperature, and pressure, can be obtained if the function of the entropy is known. An isolated system is usually not very interesting to study from an experimental point of view. However, there are more useful ensembles, like the *canonical ensemble* which is a closed and isothermal system, where the number of particles, volume, and temperature (T) are constant. The canonical partition function is defined as:

$$Q_{N,V,T} = \sum_i \Omega_{N,V,U_i} \mathrm{e}^{-\beta U_i} \, , \tag{2.2}$$

where the sum is over all energy levels, and $\beta = 1/(k_B T)$. There is also an ensemble representing an open and isothermal system, called the *grand canonical ensemble*, where the chemical potential (μ), volume, and temperature are constant. The grand canonical partition function is defined as:

$$\Xi_{\mu,V,T} = \sum_i Q_{N_i,V,T} \mathrm{e}^{-\beta\mu N_i} \,, \tag{2.3}$$

where the sum is over all number of particles. Another useful ensemble is the *isobaric ensemble*, where the number of particles, pressure (P), and temperature are constant. The isobaric partition function is defined as:

$$\Delta_{N,P,T} = \sum_i Q_{N,V_i,T} \mathrm{e}^{-\beta P V_i} \,, \tag{2.4}$$

where the sum is over all volumes. The above mentioned ensembles are all utilized in computer simulations, and it is possible to compare simulations with experimental observation. For instance, from the canonical partition function, the average pressure within the canonical ensemble can be calculated and compared with experimentally measured swelling pressure from a closed test cell. By considering the probability, ρ_i, of state with energy U_i defined as:

$$\rho_i = \frac{\mathrm{e}^{-\beta U_i}}{Q_{N,V,T}} \,, \tag{2.5}$$

the average pressure within the canonical ensemble, $\langle P \rangle$, can then be found by:

$$\langle P \rangle = \sum_i P_i \rho_i \,, \tag{2.6}$$

where the sum is over all states, and $P_i = -\frac{\delta U_i}{\delta V}$ is the pressure of the i:th configuration. Furthermore, the *Helmholtz free energy* has a similar connection within the canonical ensemble as the entropy (Eq. (2.1)) within the microcanonical ensemble, and is expressed as:

$$A = -k_B T \ln Q_{N,V,T} \,. \tag{2.7}$$

At equilibrium, the Helmholtz free energy is minimized, and if the Helmholtz free energy of the system is known, the average pressure can be calculated as:

$$\langle P \rangle = -\left(\frac{\delta A}{\delta V}\right)_{T,N} \,. \tag{2.8}$$

Note that the equation above (Eq. (2.8)) and Eq. (2.6) are equivalent.

2.4 Classical statistical mechanics

For the calculation of the partition function in the classical approach, the set of states at the quantum level is replaced by the classical continuum approach. For instance, the classical version of the canonical partition function (Eq. (2.2)) is given by:

$$Q_{class} = \frac{1}{N!\Lambda^{3N}} \int_V \mathrm{e}^{-\beta U(\Gamma)} \mathrm{d}\Gamma \,, \tag{2.9}$$

where Γ is a $3N$-dimensional vector describing the x, y, and z coordinates of particle N in the system, $U(\Gamma)$ is the systems potential energy as a function of the particles positions, Γ, and the integral is over the entire volume available to each particle. The kinetic contribution of the system is integrated and included in the de Broglie wavelength, Λ. The pressure in Eq. (2.6) can now be written as:

$$\langle P \rangle = \frac{\int_V P(\Gamma) \mathrm{e}^{-\beta U(\Gamma)} \mathrm{d}\Gamma}{Z_N} \,, \tag{2.10}$$

where $Z_N = \int_V \mathrm{e}^{-\beta U(\Gamma)} \mathrm{d}\Gamma$ is the *configurational integral*, and $P(\Gamma)$ is the pressure as a function of the particle positions, Γ.

3. Molecular interactions

3.1 Intermolecular interactions

The molecular interactions within a system can be divided into intra- and intermolecular interactions. The intramolecular interactions describe the interactions within a molecule, such as the chemical bonds, whereas the intermolecular interactions describe the interactions between molecules or colloidal particles. The intricate balance between attractive and repulsive forces are used to understand why colloidal dispersions are formed under some circumstances and why flocculation occurs in other cases. Thus, the intermolecular interactions provide information about the structural and thermodynaimcal properties of a colloidal system. For large systems it is not possible to include all particles when trying to capture the different behaviors. Hence, approximations and simplifications are made. For instance, in a 'realistic' colloidal system, the colloidal particles are dispersed in a solvent composed of a large number of particles, and to reduce the number of particles in the system the solvent is usually treated implicitly as a continuum throughout space.

3.2 Coulomb interactions

The electrostatic interaction in vacuum between two isolated charged particles i and j at a fixed distance, r_{ij}, is described by Coulomb's law:

$$u(r_{ij}) = \frac{q_i q_j}{4\pi\epsilon_0 r_{ij}} \,, \tag{3.1}$$

where q_i is the charge of particle i, and $\epsilon_0 \approx 8.854 \cdot 10^{-12}$ C^2/(Jm) is the permittivity of vacuum. If the two particles are immersed in a polar solvent, e.g. water, the pair interaction is then given by:

$$\beta w(r_{ij}) = \beta \frac{q_i q_j}{4\pi\epsilon_0\epsilon_r(T) r_{ij}} = \frac{l_B z_i z_j}{r_{ij}} \,, \tag{3.2}$$

where $l_B = \beta e^2/(4\pi\epsilon_0\epsilon_r(T))$ is the Bjerrum length, $\beta = 1/(k_B T)$ where k_B is the Boltzmann constant and T is the absolute temperature, e is the elementary charge, $z_i = q_i/e$ is the valency of particle *i*, and $\epsilon_r(T)$ is the relative permittivity of the solvent, which is dependent on the temperature (Israelachvili (2011)). In Eq. (3.2), the interactions with the solvent molecules are averaged, i.e. the solvent is treated implicity, and thus the pair interaction is a free energy. The Bjerrum length is the separation between the two charged particles at which the electrostatic interaction is equivalent to the thermal energy, $k_B T$, and if the solvent is water, the Bjerrum length increases with temperature due to the temperature-dependent relative permittivity.

3.3 Poisson-Boltzmann equation

The Poisson-Boltzmann (PB) equation describes, among other things, how colloidal dipersions are formed from charged colloids and how the intermolecular electrostatic interactions changes by additional salt. It is given by a combination of the Poisson's equation and the Boltzmann distribution according to:

$$\epsilon_r\epsilon_0 \nabla\Phi(\mathbf{r}) = -\sum_i q_i c_i \mathrm{e}^{-\beta q_i \Phi(\mathbf{r})} \,, \tag{3.3}$$

where ∇ is the Laplace operator, $\Phi(\mathbf{r})$ is the *mean* electrostatic potential at position $\mathbf{r}$, and c_i is the concentration of the ionic species *i* with charge q_i. In the PB equation a mean-field approximation is implemented, i.e. the true ion distribution is replaced by its mean distribution, and the mean electrostatic potential is defined as the average value of the potential distribution at each position in space over a long time. At low electrostatic potential, the linearized PB equation is valid, and for a spherical geometry, the solution of the interaction potential between two charged particles is:

$$\beta w(r_{ij}) = l_B z_i z_j \frac{\mathrm{e}^{-\kappa r_{ij}}}{r_{ij}} \,. \tag{3.4}$$

Here $1/\kappa$ is the Debye screening length, where $\kappa^2 = 4\pi l_B \sum_i z_i^2 c_i$ (Evans & Wennerström (1999)). From the linearized PB equation, the additional salt in a system is described as the Coulomb's law (Eq. (3.1)) multiplied with $\mathrm{e}^{-\kappa r_{ij}}$, and thus, the long-ranged electrostatic interaction between charged particles is effectively screened

by salt. For an increase in salt concentration or the valency of the salt, the electrostatic interaction becomes more short-ranged, i.e. the Debye screening length decreases (Fig 3.1).

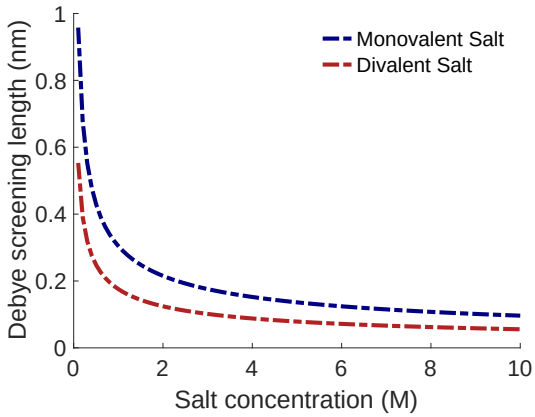

Figure 3.1: The Debye screening length ($1/\kappa$) as a function of salt concentration for a monovalent (blue dash-dotted line) and a divalent (red dash-dotted line) salt.

Moreover, for a system with two equally charged surfaces in the salt-free case, i.e. only counterions are present, the PB equation can be solved exactly. In this case, the osmotic pressure, Π, is equal to the pressure, P, and given by the so-called mid-plane approach (Evans & Wennerström (1999)),

$$\Pi_{PB} = P_{PB} = k_B T c(0) \tag{3.5}$$

where $c(0) = 2k_BTs^2\epsilon_r\epsilon_0/(zeh)^2$ is the counterion concentration at the mid-plane, s represents a dimensionless parameter, i.e. $s\tan(s) = |\sigma|zeh/(2k_BT\epsilon_r\epsilon_0)$, h is the separation between the charged surfaces, σ is the surface charge density which is smeared out on each surface, and z is the valency of the counterions. According to the PB equation, the pressure between two equally charged surfaces will always be positive, resulting in a repulsive force. On the other hand, it is possible to obtain a negative osmotic pressure, and thus, an attractive force at short separations between two highly charged particles mediated by multivalent ions if the ion-ion correlation forces are taken into account (Jönsson & Wennerström (2001)). However, these are not included in the PB equation.

3.4 Coupling theory

The coupling theory is useful for understanding the interaction within a system of two equally charged surfaces with respect to either weak or strong coupling (SC). In the limit of weak coupling, i.e. long distances between the surfaces, low surface charge, and low counterion valency, the PB equation is asymptotically exact. For the opposite limit, i.e. short distances between the surfaces, high surface charge, and high counterion valency, the SC theory is asymptotically exact. The limits can be found by considering the coupling parameter,

$$\Xi = 2\pi z^3 l_B^2 \sigma_s \,, \tag{3.6}$$

where σ_s is the surface charge number density. The PB equation is valid for small values of Ξ and the SC theory is valid for $\Xi \to \infty$, i.e. the SC limit. Moreover, the SC theory is valid if the lateral distance, α, between the ions is greater than the separation, h, between the surfaces, i.e. $h < \alpha$, where the ions almost move independently along the vertical direction due to the strong ion-ion correlation forces (Fig. 3.2a) (Netz (2001)). The PB equation is valid in systems where each ion interacts with a diffuse cloud of other ions (Fig. 3.2b).

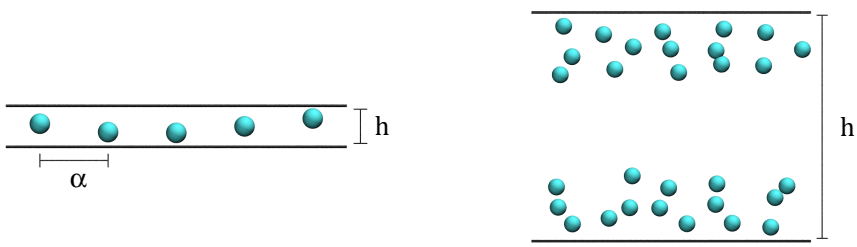

Figure 3.2: Schematic illustration of two charged surfaces (represented as horizontal black lines) mediated by counterions (represented as cyan spheres). (a) The lateral distance, α, between the ions is greater than the separation, h, between the charged surfaces. (b) The charged surfaces attract two separate layers of counterions, where the lateral distance between the ions is small. (Jansson et al. (2018))

3.5 Short-ranged interactions

In addition to the long-ranged electrostatic interactions, particles also exhibit short-ranged interactions. The principle of the short-ranged interactions implies that two interacting particles repel each other at close distances. This originates from the Pauli

exclusion principle which states that two or more identical electrons can not occupy the same quantum state. The *hard-sphere* (HS) potential and the *truncated and shifted Lennard-Jones* (TLJ) potential are two simple potentials that describe this interaction (Fig. 3.3). The hard-sphere potential between two particles *i* and *j* is defined as:

$$u(r_{ij}) = \begin{cases} +\infty & \text{if } r_{ij} < \sigma_{ij} \\ 0 & \text{otherwise} \end{cases} , \tag{3.7}$$

where $\sigma_{ij} = (d_i + d_j)/2$, and d_i is the diameter of particle *i*. The truncated and shifted Lennard-Jones potential is strictly repulsive and defined as:

$$u(r_{ij}) = \begin{cases} \epsilon \left((\frac{\sigma_{ij}}{r_{ij}})^{12} - 2(\frac{\sigma_{ij}}{r_{ij}})^{6} + 1 \right) & \text{if } r_{ij} < \sigma_{ij} \\ 0 & \text{otherwise} \end{cases} , \tag{3.8}$$

where ϵ determines the strength of the interaction. Moreover, there is also an attraction between the particles which is described by the van der Waals forces. These are a collection of interactions proportional to r^{-6} and originates from (i) the Keesom force for the rotational average between two dipoles, (ii) the Debye force for the rotational average between a dipole and a corresponding induced dipole, and (iii) the London dispersion force considering the instantaneous induced dipole. By combining the Pauli exclusion principle with the van der Waals forces, the *Lennard-Jones* (LJ) potential is obtained and defined as:

$$u(r_{ij}) = 4\epsilon \left((\frac{\sigma_{ij}}{r_{ij}})^{12} - (\frac{\sigma_{ij}}{r_{ij}})^{6} \right) . \tag{3.9}$$

The minimum value of the potential is found at $r_{ij} = 2^{1/6}\sigma_{ij}$ (Fig. 3.3). The theory of describing the electrostatic interactions with the linearized PB equation and the short-ranged interactions with the van der Waals forces is known as the DLVO-theory (Derjaguin & Landau (1941); Verwey & Overbeek (1948)).

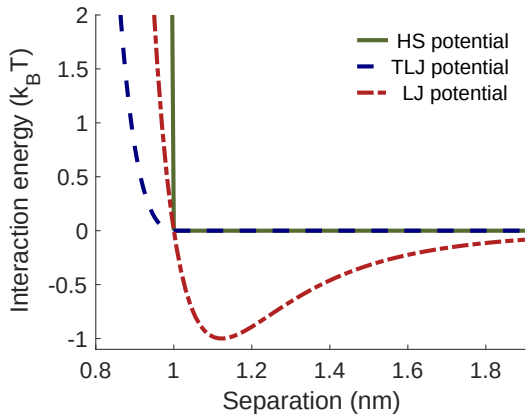

Figure 3.3: An comparison between the short-ranged interaction potentials, with $\epsilon = 1\ k_BT$ and $\sigma = 1$ nm, for the hard-sphere (HS) potential (green solid line), the truncated and shifted Lennard-Jones (TLJ) potential (blue dashed line), and the Lennard-Jones (LJ) potential (red dash-dotted line).

4. Simulation techniques

4.1 Coarse-grained modeling

In a coarse-grained model, the description of a system is simplified by reducing the number of degrees of freedom, thereby reducing the complexity of the system. The advantage of this approach is that it is possible to study large-scale systems at a reduced computational cost, in contrast to atomistic models. On the other hand, it is usually not possible to obtain a quantitative agreement with experiments. Instead, a qualitative correspondence can be captured where the overall trends can be understood. To represent a colloidal particle as an coarse-grained model, a set of atoms is replaced by a coarse-grained site, where the resolution of the model depends on the number of atoms within the set. Bonded interactions, like harmonic stretching potentials and/or harmonic angle potentials, are used to connect the sites with each other and maintain their shape. The interactions between the coarse-grained sites consists of non-bonded effective pair-potentials, where the parameters have been chosen from either a more detailed model and/or experimental data.

The coarse-grained models used in this thesis are at the level of the *primitive model* (Linse (2005)), i.e. all of the charged species are treated as charged hard or soft spheres, and the solvent is treated implicity through the relative permittivity and regarded as temperature dependent.

4.2 Clay platelets and ions

The clay platelets have been described with two different coarse-grained models in this thesis. In the first model, two negatively charged planar surfaces are used to mimic two parallel clay platelets. The surfaces have a uniform charge with a surface charge density σ, and are neutralized with mobile counterions with a diameter of 0.4 nm (Fig. 4.1). The system takes into account both ion-surface interactions and ion-ion

pairwise interactions, where the latter is described by a combination of Eq. (3.2) and Eq. (3.7). The simulation box is finite with length L in the directions parallel to the surfaces and the surfaces are separated by a distance h, hence, the volume is equal to $V = hL^2$. *Periodic boundary conditions* are implemented for the ions, i.e. if an ion moves outside the box ($x > L/2$) in the direction parallel to the surfaces, the ion will reappear at $x = x - L$. The distance between two ions is calculated by the *minimum image convention*, i.e. if $r_x > L/2$ then $r_x = |r_x - L|$. Moreover, the long-ranged interactions outside the box is accounted for by implementing an external potential.

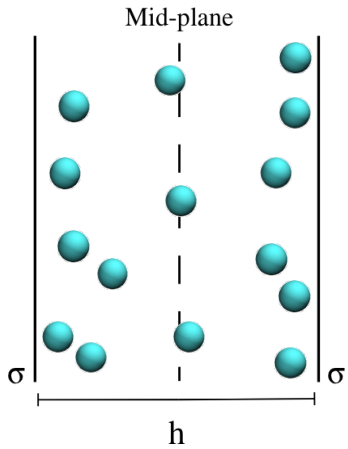

Figure 4.1: A schematic illustration of the first model. Two parallel clay platelets are coarse-grained as two negatively charged planar surfaces with surface charge density σ (represented as the two vertical black lines), and neutralized by mobile counterions (represented as cyan spheres). The mid-plane is represented as the dashed black line.

For the second model, a clay platelet is represented as a finite hexagonal monolayer of connected coarse-grained spheres, denoted as sites (Fig. 4.2). The volume fraction of the system is defined as:

$$\phi = \frac{4\pi r^3 N_p N_s}{3V}\,, \tag{4.1}$$

where $r = 0.5$ nm is the radius of a site, N_p is the number of platelets, N_s is the number of sites per platelet, and V is the volume of the simulation box. A total electrical charge of Q_p unit charges is equally distributed among the sites, where each site holds $Q_s = Q_p/N_s$ unit charges, located in the center of the site. The surface charge density is estimated from an infinite plane of sites arranged in a hexagonal pattern, i.e. $\sigma_s = Q_s \cdot \frac{2}{\sqrt{3}}$. All adjacent sites within the platelet are connected by a harmonic bond-stretching potential,

$$u_b(r_{ij}) = \frac{1}{2} k^b (r_{ij} - b)^2 \,, \tag{4.2}$$

where k^b is the force constant, r_{ij} is the separation between site i and j, and $b = 1$ nm is the equilibrium bond length. Furthermore, the flexibility of the platelet is constrained by an harmonic bending potential between triplets of bonded sites,

$$u_a(\theta_{ijk}) = \frac{1}{2} k^\theta (\theta_{ijk} - \theta^\circ)^2 \,, \tag{4.3}$$

where k^θ is the force constant, θ_{ijk} is the bond angle between the sites i, j and k, and $\theta^\circ = \pi$.

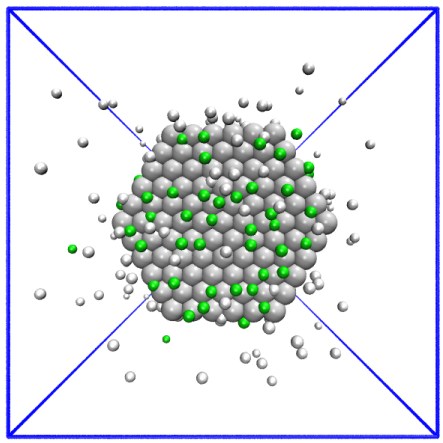

Figure 4.2: A schematic picture of the second coarse-grained model. The clay platelet is represented as a finite hexagonal monolayer of connected charged spheres (grey plate), the mono-, and divalent counterions are modeled as freely moving charges (white and green spheres), and the cubic simulation box is defined as the blue box.

The counterions are modeled as freely moving charges with a diameter of 0.4 nm, and the platelet charge is neutralized by either mono-, and/or divalent cations. In Paper 1, the fraction of divalent counterion charge ratio was defined as:

$$\eta_{\mathrm{Di}} = \frac{2N_{\mathrm{Di}}}{2N_{\mathrm{Di}} + N_{\mathrm{Mon}}} \,, \tag{4.4}$$

where N_{Mon}, and N_{Di} is the number of mono-, and divalent counterions respectively. All of the particles within the system, except adjacent platelet sites, interact pairwise by combining Eq. (3.2) with Eq. (3.7) or Eq. (3.8).

4.3 Simulation methods

In classical statistical mechanics, the most commonly used simulation methods are Monte Carlo (MC) and Molecular Dynamics (MD) simulations. The advantage by using simulations over analytical solutions obtained from theory is that the latter contains a large number of approximations and are limited to small and simple systems. However, the disadvantage is that if the model is too complex and involves to many parameters, it can be hard to gain the physical insight of the system. The difference between MD and MC simulations can be explained by consider the ergodic hypothesis; *(i) the average value of a certain property after a long time is equal to (ii) the ensemble average*. The former, (i), is considered in MD simulations, where the dynamics of the system is captured due to that the particles move according to Newton's law of motion, and hence, the average value of a property is found after a long time. The latter, (ii), is described by the MC simulations, where the concept of time is absent and instead a large number of configurations are considered within the ensemble, and the average value of a property is found by the ensemble average.

4.4 Monte Carlo simulations

For Monte Carlo, the system is described from the ensemble average. The straightforward MC technique is the random sampling or brute force MC, where the particles coordinates are randomly chosen for a large set of configurations. The disadvantage with this approach is that it is very inefficient for dense systems, since the majority of the generated configurations will not contribute significantly to the average. For a randomly generated configuration in dense systems, there is a high probability that the coordinates of the particles will overlap. This will increase the energy of the configuration due to short-ranged repulsive interactions, and thus, the total energy of a dense system will be above k_BT, i.e. $\mathrm{e}^{-\beta U(\Gamma)} \gg 1$. A more efficient and robust approach is to implement *importance sampling*, in which the majority of the configurations are sampled in the region of space where it will contribute significantly to the average. One of the most recognized importance sampling techniques is the Metropolis method.

4.4.1 Metropolis method

The Metropolis method (Metropolis et al. (1953); Allen & Tildesley (1989)) is a sampling method in Monte Carlo simulations for dense and more complex systems. The generated configurations are proportional to the Boltzmann weight and described by the probability density, $\rho = \mathrm{e}^{-\beta U(\Gamma)}/Z_N$, where Γ is the probability coordinates of the

configuration. For a system to reach equilibrium, the criterion of *detailed balance* is introduced,

$$\rho_{\mathrm{o}}\pi_{\mathrm{o}\to\mathrm{n}} = \rho_{\mathrm{n}}\pi_{\mathrm{n}\to\mathrm{o}}\,, \tag{4.5}$$

where $\pi_{\mathrm{o}\to\mathrm{n}}$, and $\pi_{\mathrm{n}\to\mathrm{o}}$ are the transition probability densities from the old to the new configuration, and vice versa. In the Metropolis scheme, the detailed balanced is fulfilled by the following condition:

$$\pi_{\mathrm{o}\to\mathrm{n}} = \begin{cases} \gamma_{\mathrm{o}\to\mathrm{n}} & \text{if } \rho_{\mathrm{n}} \geq \rho_{\mathrm{o}} \\ \gamma_{\mathrm{o}\to\mathrm{n}} \cdot \alpha & \text{if } \rho_{\mathrm{n}} < \rho_{\mathrm{o}} \end{cases}, \tag{4.6}$$

where $\gamma_{\mathrm{o}\to\mathrm{n}} = \gamma_{\mathrm{n}\to\mathrm{o}}$ describes a symmetric random *trial move*, and α is the acceptance ratio from an old to a new configuration. The trial moves in MC simulations have no physical meaning, and there is a vast number of trial moves optimized for different type of systems. For instance, the *single particle displacement* is a trial move where a single particle is chosen randomly and translated or rotated randomly. For translation of a single particle, the random trial move describes the uniform probability of the particle movement in any direction within a maximum allowed distance. The symmetry arises from that the probability of finding a certain new position is equal to find the old position when the particles are at the new positions. By rewriting Eq. (4.5) the acceptance ratio is described as:

$$\alpha = \frac{\pi_{\mathrm{o}\to\mathrm{n}}}{\pi_{\mathrm{n}\to\mathrm{o}}} = \frac{\rho_{\mathrm{n}}}{\rho_{\mathrm{o}}} = \frac{\mathrm{e}^{-\beta U(\Gamma_{\mathrm{n}})}}{Z_N} \frac{Z_N}{\mathrm{e}^{-\beta U(\Gamma_{\mathrm{o}})}} = \mathrm{e}^{-\beta(U(\Gamma_{\mathrm{n}}) - U(\Gamma_{\mathrm{o}}))}\,. \tag{4.7}$$

The advantage with the Metropolis method is that unphysical moves are possible. However, the disadvantage is that a new configuration can only be generated if the previous configuration is known. Thus, an initial configuration of the particle positions is needed, where the geometry and boundary conditions of the system are defined. The following steps can be used to describe the method,

1. A random trial move is selected.
2. A random particle or set of particles as required by the trial move is selected and the move is performed to generate a new configuration.
3. The acceptance ratio is calculated and the new configuration is accepted if $\alpha \leq 1$ (when $\rho_{\mathrm{n}} \geq \rho_{\mathrm{o}}$) or $\alpha > R$ (when $\rho_{\mathrm{n}} < \rho_{\mathrm{o}}$), where R is a random number between zero and one, otherwise the new configuration is rejected.

4. The observables of interest is sampled when the system has reached equilibrium.
5. The scheme is repeated from step 1.

4.5 Molecular dynamics simulations

In molecular dynamics simulations the particles of the system move according to Newton's laws of motion. The advantages with MD is that it captures the dynamics of the system. Furthermore, parallelization is straightforward and the algorithms are universial for most type of systems. The disadvantage, however, is that it takes a long time for the system to cross energy barriers much larger than $k_B T$, and it requires that interaction forces are continuous for most MD packages (e.g. GROMACS (Pronk et al. (2013); Abraham et al. (2014))).

Newton's second law of motion states that the force **F** acting on a particle is equal to the product of the particles mass m and acceleration **a**, i.e. $\mathbf{F} = m\,\mathbf{a}$, assumed that the mass is constant. For a system with many particles, the force acting of particle i at time t is:

$$\mathbf{F}_i(t) = \sum_{j \neq i} \nabla u_{ij}(|\mathbf{r}_i(t) - \mathbf{r}_j(t)|) = -\sum_{j \neq i} \nabla u_{ij}(r_{ij}(t))\,, \tag{4.8}$$

where the sum is over all particles except particle i itself, $\mathbf{r}_i(t)$ is the position of particle i at time t, and $u_{ij}(\mathrm{r})$ is the pair potential between particles i and j. For numerical integration of the equation of motion, the Velocity Verlet algorithm can be used, where the particles inital position and velocity at time t is defined. The Velocity Verlet algorithm can be described in the following steps,

1. The particles position at time $t + \delta t$ is calculated according to:

$$\mathbf{r}(t + \delta t) = \mathbf{r}(t) + \mathbf{v}(t)\delta t + \frac{\mathbf{a}(t)}{2}\delta t^2\,, \tag{4.9}$$

   where δt is the timestep, $\mathbf{a}(t) = \mathbf{F}(t)/m$ is the acceleration obtained from Eq. (4.8), $\mathbf{v}(t)$ is the velocity, and $\mathbf{r}(t)$ is the position of the particle.

2. $\mathbf{a}(t + \delta t)$ is calculated for the particle position $\mathbf{r}(r + \delta t)$.

3. The velocity of the particle at time $t + \delta t$ is calculated as:

$$\mathbf{v}(t + \delta t) = \mathbf{v}(t) + \frac{\mathbf{a}(t) + \mathbf{a}(t + \delta t)}{2}\delta t\,. \tag{4.10}$$

4. The algorithm is repeated from step 1 to find the position of the particles at time $t + 2\delta t$.

In MD integrators, the number of particles, the volume and the energy of a system are conserved if the timestep, δt, is small enough, i.e. it represents the microcanonical ensemble. For simulations of a system within the canonical or isobaric ensemble, thermostats (Berendsen et al. (1984); Nosé (1984); Hoover (1985); Bussi et al. (2007)) and barostats (Parrinello & Rahman (1981); Nosé & Klein (1983); Berendsen et al. (1984)) are implemented. For a more detailed description of the methods the reader are refeered to the above mentioned references.

4.6 Boundary conditions

For simulations to represent a 'realistic' system, the simulation box has to contain a great number of particles which would be too complex to simulate, and also too expensive with respect to the computational resources available. To circumvent this issue, some type of boundary conditions are necessary to implement to limit the size of the system. For instance, *periodic boundary conditions* are a set of boundary conditions where a large system is approximated by a small model system, i.e. a unit cell. The periodicity ensures that the system is unaffected at the boundaries, and the conditions mimics the presence of an infinite bulk surrounding the unit cell. For a cubic simulation box, the periodic boundary conditions implies replicates of the cubic unit cell in all directions, yielding a periodic infinite lattice throughout space (Fig. 4.3). The replicates are identical images of the unit cell, hence, if a particle moves outside the unit cell, one of its images will enter the unit cell from the opposite face.

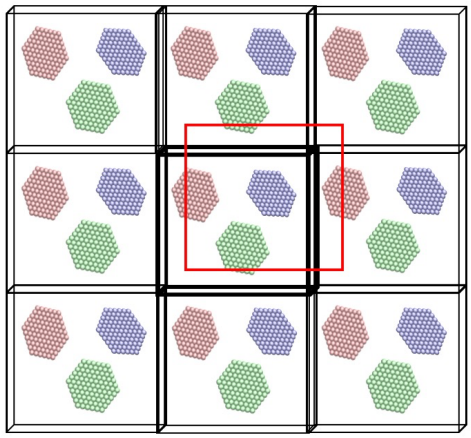

Figure 4.3: A schematic illustration of a system with periodic boundary conditions where all particles are located in the central cubic unit cell which is replicated in all directions. Applying minimum image convention corresponds to a cubic cut-off represented as the red box.

4.7 Minimum image convention

For a system with periodic boundary conditions the cubic unit cell is placed in an imaginary infinite lattice of images. By considering all the interactions within the system it would result in an infinite sum due to that the system is composed of an infinite number of particles. To restrict this, an approximation over the possibility of truncating the potentials is made by applying *minimum image convention*. The approach of minimum image convention states that each particle only interacts with the closest image of the other particles, and thus, corresponds to a cubic cut-off (Fig. 4.3).

5. Experimental methods

5.1 Bentonite clay - purification and cationic exchange

The type of raw clay used in this thesis was MX-80, a bentonite from Wyoming, Montana and/or South Dakota in the USA. This clay is mainly composed of the swelling clay mineral montmorillonite with sodium (Na^+) ions as natural dominating counterion.

Purification of raw bentonite clay is necessary to ensure that the majority of the accessory minerals (e.g. feldspars, quartz, gypsum, calcite and pyrite), are removed. This can be achieved by dispersing the raw clay in deionized water for at least one day to allow the larger particles (> 2 μm) to sediment, and afterwards recover the supernatant. For the cationic exchange, the clay is washed three times with a salt solution of either 1 M NaCl, or 0.5 M $CaCl_2$ in order to exchange the counterions to sodium or calcium, respectively. To remove the excess salt, the clay suspension is dialyzed in a large reservoir of deionized water, which is frequently replaced until the electrical conductivity is stabilized below 10 μS/cm.

The purification and cationic exchange of MX-80 were adapted for the studies in both Paper I and Paper II, in which the clay is denoted X-montmorillonite and X-mmt, respectively, where X is either Na^+ or Ca^{2+}, and mmt is the abbreviation of montmorillonite.

5.2 Small angle X-ray scattering

Small angle X-ray scattering (SAXS) is a technique appropriate to study the microstructure of systems of the colloidal scale. For clay systems, the information extracted from SAXS is usually the platelet size, the interlayer distance between the platelets, the size of the aggregates, i.e. the number of clay platelets per aggregate, and the fractal dimen-

sions. The principle of the SAXS technique is that a coherent monochromatic beam of X-rays with wavelength, λ, is sent through a sample with an incident wavevector, $\mathbf{k}_i$, and the outgoing scattered beam has wavevector $\mathbf{k}_s$. The scattering intensity, $I(q)$, is recorded as a 2D interference pattern on a detector, and is represented as a function of the magnitude of the scattering vector q, where $q = |\mathbf{q}| = |\mathbf{k}_s - \mathbf{k}_i| = 4\pi \sin(\theta)/\lambda$, and 2θ is the scattering angle (Glatter & Kratky (1982)). The technique is schematic illustrated in Fig. 5.1.

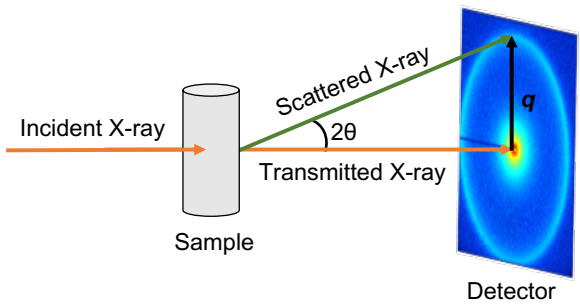

Figure 5.1: A schematic illustration of the SAXS technique and the main components. An incident beam is sent through a sample, the scattering angle between the transmitted and the scattered beam is denoted 2θ, and the corresponding q-vector is shown on the 2D detector.

The scattering intensity for systems with spherical particles can be divided into two separate functions, the form factor $P(q)$, and the structure factor $S(q)$, according to $I(q) \propto P(q)S(q)$. The form factor contains information about the average particle size and shape, and the structure factor describes the distances between the particles, and the intermolecular interactions in the system. For dilute systems, the form factor can be extracted since $S(q) \approx 1$, and once the form factor of the system is known, the structure factor for more dense systems can be determined provided that the form factor is concentration independent (Schnablegger & Singh (2017)). For anisotropic particles, such as clay platelets, the decomposition of the scattering intensity is an approximation, and a more accurate description of the system can be performed by comparing the experimental scattering intensity with the calculated *total structure factor* (Gutiérrez & Johansson (2002)) from computer simulations.

For the structural configuration of stacked platelets, where the clay platelets aggregate in a face-to-face configuration, Bragg peaks are present in the SAXS spectra due to the periodicity of the system, which arises from the equdistant separation between the platelets. The interlayer distance can be determined from Bragg's law: $d = 2\pi/q_{max}$, where q_{max} is the position of q at the maximum intensity of the Bragg peak (Schnablegger & Singh (2017)). Moreover, the full width at half maximum (FWHM) of the Bragg peak is related to the size of the aggregates, which is determined from the aver-

age number of platelets per tactoid, $\langle N \rangle$, according to the Scherrer equation (Patterson (1939)):

$$\langle N \rangle d = \frac{K\lambda}{\Delta\theta \cos(\theta)}\,, \tag{5.1}$$

where $K \approx 0.9$ is the Scherrer constant, $\Delta\theta = \theta_2 - \theta_1$ is the FWHM of the Bragg peak between the angles θ_1 and θ_2, and 2θ is the Bragg angle. For small angles, the FWHM of the Bragg is $\Delta\theta \approx \sin(\theta_2) - \sin(\theta_1)$ and the Scherrer equation can be approximated as,

$$\langle N \rangle \approx \frac{q_{max}}{2\pi(\sin(\theta_2) - \sin(\theta_1))/\lambda} = \frac{q_{max}}{(\Delta q)/2} = \frac{q_{max}}{w}\,. \tag{5.2}$$

Here the Scherrer constant is set to one, and $\Delta q = 2w$ is the FWHM in units of nm^{-1}. The method used to estimate the FWHM of the Bragg peak was to fit a Lorentzian function to the structure factor, where it is assumed that the scattering intensity can be divided into $P(q)$ and $S(q)$. Also, the form factor is approximated to be $P(q) \propto q^{-2}$, and the data was fitted between $q_{max} = \pm\, 0.5$ nm^{-1} (Segad (2013); Thuresson et al. (2016)),

$$q^2 I(q) \propto \frac{w}{(q - q_{max})^2 + w^2} + b\,, \tag{5.3}$$

where b is a fitting parameter for the background contribution. This method can describe the size of the aggregate for clay platelets with a large aspect ratio and with relative narrow Bragg peaks. Hence, this method has proven to be accurate for montmorillonite clay.

5.3 Swelling pressure in a test cell

The swelling pressure, or the net osmotic pressure, of clay in water and different solvent compositions can be directly measured using a test cell (Karnland et al. (2006); Birgersson et al. (2010)). The experimental setup and a schematically depicted test cell are shown in Fig. 5.2. The clay, with a mass of approximately one gram, is placed inside a cylindrical cell with a radius of 1 cm and enclosed by two semi-permeable membranes at the top and bottom of the cell. The function of the semi-permeable membranes is that the water and ions are allowed to freely diffuse between the two compartments while the clay is retained. Then, the clay is confined in a predefined volume by a piston,

which is attached to a force transducer, and the clay is set to equilibrate with water or the solvent composition of interest by slowly circulating the bulk solution through the test cell via the connected tubes. From the recorded force, F, and the area of the cell, $A = 0.01^2\pi$ m^2, the swelling pressure of the system is calculated as $P = F/A$ N/m^2. By measuring the force over time, it is possible to find a stable value of the swelling pressure for the clay sample with a certain solvent composition, where the clay is assumed to be in equilibrium with the bulk.

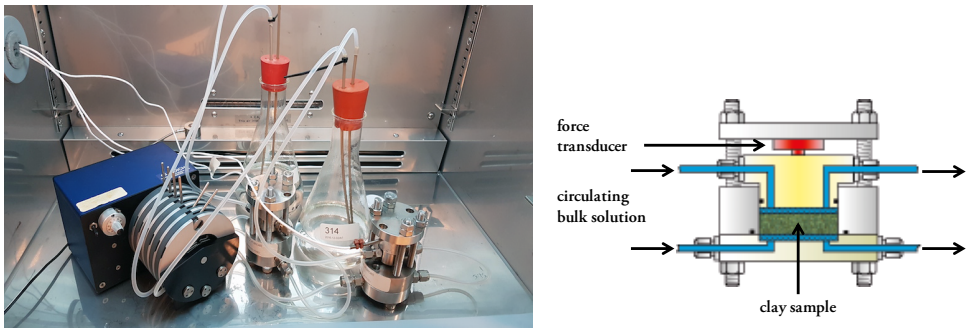

(a) (b)

Figure 5.2: (a) The experimental setup of a swelling pressure measurement, and (b) a schematic illustration of the test cell (Karnland et al. (2006))

After the measurement, the water content, $w = m_w/m_s$, of the clay sample is determined, where m_w, and m_s is the mass of the water, and solid, respectively, by disassembling the test cell and measure the total mass $m_{tot} = m_w + m_s$. The clay sample is then dried in an oven at around 100°C for 24h to recover the mass of the solid. Furthermore, from the density of the clay (montmorillonite), $D_s = 2750$ kg/m^3, and the density of water, $D_w = 1000$ kg/m^3, the dry density of the clay can be calculated from $D_d = m_s/V_{tot} = D_w/(w + D_w/D_s)$, and the volume fraction is $\phi = D_d/D_s$ (Karnland et al. (2006)).

6. The research

6.1 Main results of the research papers

A short summary of the main results of each paper is presented below.

6.1.1 Paper 1: Temperature Response of Charged Colloidal Particles by Mixing Counterions Utilizing Ca^{2+}/Na^{+} Montmorillonite as Model System

In the first paper, the osmotic pressure and the aggregation of charged colloids as a function of temperature were investigated by using coarse-grained molecular dynamics bulk simulations, and Monte Carlo simulations of two infinite parallel surfaces for different ratios of mono- and divalent counterions. The model system was Ca^{2+}/Na^{+}-montmorillonite, and the different counterion charge ratios were obtained by successively exchanging the sodium ions with calcium ions. It was found that the temperature response can be controlled, and that the electrostatic interactions alone can give a positive, negative, or constant osmotic pressure response with temperature, depending on the counterion charge ratio. The increase in osmotic pressure with temperature, which occurs at a low fraction of divalent counterions, can be explained by the DLVO-theory, and the origin of the opposite behavior can be explained by the enhanced attractive electrostatic ion-ion correlation interactions with temperature. Moreover, the microstructural characterization of Ca^{2+}/Na^{+}-montmorillonite at different counterion charge ratios was studied by SAXS, where the theoretical predictions of the temperature response are in qualitative agreement with the experimental data, indicating that the models can explain the underlying physics.

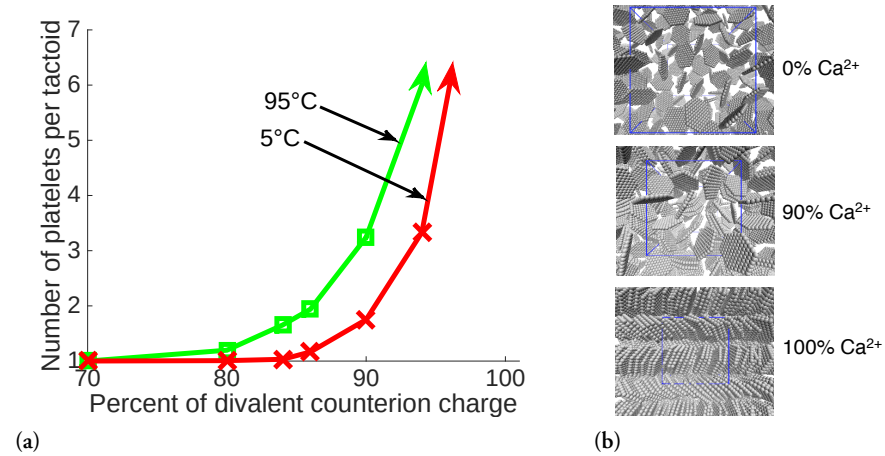

Figure 6.1: (a) Number of platelets per tactoid as a function of divalent counterion charge ratio in percent, and (b) illustrative representations of the structure for the systems with 0, 90, and 100% fraction of divalent ions.

6.1.2 Paper II: The Effect of the Relative Permittivity on the Tactoid Formation in Nanoplatelet Systems. A Combined Computer Simulation, SAXS, and Osmotic Pressure Study

In the second paper, the structural and swelling properties of sodium and calcium saturated montmorillonite (Na-, and Ca-mmt) were studied as an effect of decreasing the relative permittivity of the solvent by using water and ethanol mixtures. The experimental techniques, SAXS and osmotic pressure measurements in combination with coarse-grained molecular dynamics bulk simulations, Monte Carlo simulations of two infinite parallel surfaces, and the strong coupling theory were utilized. For Na-mmt, it was found, both experimentally and theoretically, that tactoids were formed when decreasing the relative permittivity of the solvent, indicating that it is possible to tune the electrostatic interactions to obtain a transition from a repulsive to an attractive system via the solvent properties. This effect arises from the increase in Bjerrum length and can be qualitatively explained by the coupling parameter, where the decrease in the relative permittivity gives rise to a stronger coupling, and thus, the attractive ion-ion correlation forces are enhanced. Moreover, for Ca-mmt, a non-monotonic swelling behavior was captured experimentally, where the osmotic pressure and the interlayer distance between the platelets first increased and then decreased as a function of the relative permittivity of the solvent. The former indicates that repulsive short-ranged interactions dominate in the system, and the latter implies that ion-ion correlation forces are of importance. Theoretically, the non-monotonic behavior could not be captured with the continuum model, probably due to the limitation that the electrostatic interactions solely enters the Hamiltonian via the Bjerrum length.

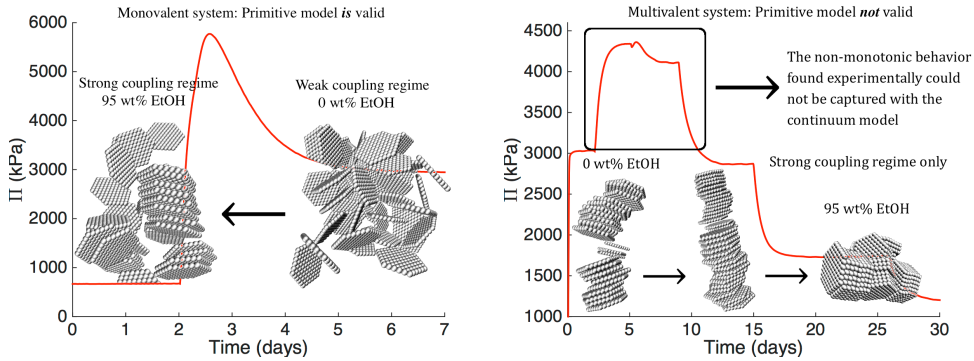

Figure 6.2: (a) The osmotic pressure response of Na^+-montmorillonite, with illustrative configurations corresponding to 95 (left), and 0 (right) wt% ethanol. (b) The osmotic pressure response of Ca^{2+}-montmorillonite, where the black box represents the limitation regime of the continuum model, and the illustrative configurations correspond to 0 (left), 20 (middle), and 95 (right) wt% ethanol.

6.2 Conclusion and outlook

The overall objective in this thesis have been to try to understand the tactoid formation in the clay mineral montmorillonite with respect to the divalent counterion charge ratio and the temperature, as well as an effect of the relative permittivity of the solvent. The structure and swelling have been investigated theoretically by coarse-grained simulations of negatively charged platelets and surfaces, representing the clay platelets, and experimentally with small angle X-ray scattering and swelling pressure measurements in a test cell. The purpose of the simulations have been to try to connect theory with experimental findings where the focus has been on the electrostatic interactions within the system. My continued research will build on these findings, and also expand into the development of a more 'realistic' coarse-grained model of clay platelets where platelets with anisotropic charge, i.e. negative surface charge and positive edge charge, will be implemented. Furthermore, the structural response of clay dispersion upon addition of charged polymers will be investigated, where it is suggested that the charged polymer will promote aggregation, depending on it size and charge. These systems are of great interest to study from a clinical perspective, since clay has been suggested as a candidate for drug delivery. Hence, the overall goal is to obtain a deeper understanding of the intermolecular interactions and the structural properties for the tactoid formation of clay with additional charged polymers.

References

Abraham, M. J., van der Spoel, D., Lindahl, E., Hess, B., & the GROMACS development team. 2014, GROMACS User Manual version 5.0.4, www.gromacs.org

Allen, M. P., & Tildesley, D. J. 1989, Computer Simulation of Liquids (New York: Oxford University Press)

Bailey, S. W. 1980, Clay Minerals, 15, 85

Berendsen, H. J. C., Postma, J. P. M., van Gunsteren, W. F., DiNola, A., & Haak, J. R. 1984, The Journal of Chemical Physics, 81, 3684

Bergaya, F., Theng, B. K. G., & Lagaly, G. 2006, Developments in Clay Science, Vol. 1, Handbook of Clay Science (Elsevier)

Birgersson, M., Karnland, O., & Nilsson, U. 2010, SKB Technical Report, TR-10-40

Bussi, G., Donadio, D., & Parrinello, M. 2007, The Journal of Chemical Physics, 126, 014101

Callen, H. B. 1985, Thermodynamics and an Introduction to Thermostatistics, 2nd edn. (New York: Wiley)

Deer, W. A., Howie, R. A., & Zussman, J. 2013, An Introduction to the Rock-Forming Minerals, 3rd edn. (London: The Mineralogical Society)

Delhorme, M., Jönsson, B., & Labbez, C. 2012, Soft Matter, 8, 9691

Derjaguin, B. V., & Landau, L. 1941, Acta Physico Chemica URSS, 14, 633

Evans, D. F., & Wennerström, H. 1999, The Colloidal Domain: Where Physics, Chemistry, Biology, and Technology Meet, 2nd edn. (USA: Wiley-WHC)

Glatter, O., & Kratky, O. 1982, Small Angle X-ray Scattering (London: Academic Press)

Grim, R. E. 1953, Clay Mineralogy (New York: McGraw-Hill Book Company Inc.)

Guggenheim, S., & Martin, R. T. 1995, Clays and Clay Minerals, 43, 255

Gutiérrez, G., & Johansson, B. 2002, Physical Review B

Hedström, M., Birgersson, M., Nilsson, U., & Karnland, O. 2011, Physics and Chemistry of the Earth, Parts A/B/C, 36, 1564

Hill, T. L. 1986, An Introduction to Statistical Thermodynamics (New York: Dover Publications Inc.)

Hoover, W. G. 1985, Physical Review A, 31, 1695

Israelachvili, J. N. 2011, Intermolecular and Surface Forces, 3rd edn. (USA: Academic Press)

Jansson, M., Thuresson, A., Plivelic, T. S., Forsman, J., & Skepö, M. 2018, Journal of Colloid and Interface Science, 513, 575

Jönsson, B., & Wennerström, H. 2001, Electrostatic Effects in Soft Matter and Biophysics (Netherlands: Springer), 171–204

Karnland, O., Olsson, S., & Nilsson, U. 2006, SKB Technical Report, TR-06-30

Linse, P. 2005, Simulation of Charged Colloids in Solution (Berlin: Springer), 111–162

Metropolis, N., Rosenbluth, A. W., Rosenbluth, M. N., Teller, A. H., & Teller, E. 1953, The Journal of Chemical Physics, 21, 1087

Michot, L. J., Bihannic, I., Porsch, K., et al. 2004, Langmuir, 20, 10829

Netz, R. R. 2001, The European Physical Journal E, 5, 557

Nosé, S. 1984, Molecular Physics, 52, 255

Nosé, S., & Klein, M. L. 1983, Molecular Physics, 50, 1055

Parrinello, M., & Rahman, A. 1981, Journal of Applied Physics, 52, 7182

Patterson, A. L. 1939, Physical Review, 56

Pronk, S., Páll, S., Schulz, R., et al. 2013, Bioinformatics, 29, 845

Schnablegger, H., & Singh, Y. 2017, The SAXS Guide, 4th edn. (Austria: Anton Paar GmbH)

Segad, M. 2013, Journal of Applied Crystallography, 46, 1316

Segad, M., Cabane, B., & Jönsson, B. 2015, Nanoscale, 7, 16290

SKB. 2011, SKB Technical Report, TR-11-01

Thuresson, A., Segad, M., Turesson, M., & Skepö, M. 2016, Journal of Colloid and Interface Science, 466, 330

Verwey, E. J. W., & Overbeek, J. T. G. 1948, Theory of the Stability of Lyophobic Colloids (Amsterdam: Elsevier Publishing Company Inc.)

Acknowledgements

To summarize the first two years of my PhD studies has been a challenge, but at the same time it has felt very useful to write the most important aspects of my projects and research. Looking back at what has been done and what has been accomplished so far has been very valuable to me for my future projects and research. I have had the opportunity to collaborate with various people who have supported me throughout the projects, and I want to mention the peoples I think helped me the most.
Marie Skepö, thank you for giving me the opportunity to become a PhD student and for being my supervisor with your endless support and guidance.
Axel Thuresson, thanks for introducing me into the world of clay and for sharing all your knowledge with me, I really appreciated it.
Tomás Plivelic, thank you for all the experimental expertise and all the valuable discussions regarding data analysis and implementations, and of course for all our nice trips.
Clay Technology, thanks for allowing me to work in your lab.
Jan Forsman, thank you for all discussions and for your feedback on this thesis.
The members in our research group, thank you all for making the days so pleasant and for all the nice trips we have done as for all good discussions it has provided.
All colleagues at the Division of Theoretical Chemistry, thanks for contributing to a pleasant working environment and for all good laughs at fika.

Scientific publications

Author contributions

Paper I: Temperature Response of Charged Colloidal Particles by Mixing Counterions Utilizing Ca^{2+}/Na^{+} Montmorillonite as Model System

Involved in planning and writing the manuscript. Performed the simulations and the corresponding analyses. Planned and performed the experiments together with the co-authors.

Paper II: The Effect of the Relative Permittivity on the Tactoid Formation in Nanoplatelet Systems. A Combined Computer Simulation, SAXS, and Osmotic Pressure Study

Planned and formulated the scientific questions and hypotheses together with the co-authors. Planned, performed and analyzed all the experiments and simulations together with the co-authors. Main responsible for writing the manuscript with input from the co-authors. Responsible for the submission and the revision process.

Paper I

THE JOURNAL OF PHYSICAL CHEMISTRY C

Article

pubs.acs.org/JPCC

Temperature Response of Charged Colloidal Particles by Mixing Counterions Utilizing Ca^{2+}/Na^{+} Montmorillonite as Model System

Axel Thuresson,*[,†] Maria Jansson,[†] Tomás S. Plivelic,[‡] and Marie Skepö*[,†]

[†]Theoretical Chemistry and [‡]MAX IV Laboratory, Lund University, SE-221 00 Lund, Sweden

ABSTRACT: The osmotic pressure and the aggregation of charged colloids as a function of temperature have been investigated using Monte Carlo and molecular dynamics simulations for different ratios of monovalent and divalent counterions. In the simulations the water is treated as a temperature-dependent dielectric continuum, and only the electrostatic interactions are considered. It was found that the temperature response can be controlled, i.e., the osmotic pressure can increase, decrease, or be kept constant, as a function of temperature depending on the monovalent/divalent counterion ratio. The increase in osmotic pressure with temperature, which occurs at low enough surface charge density and/or low fraction of divalent ions, can be understood from the DLVO theory. The origin of the opposite behavior can be explained by the enhanced attractive electrostatic ion−ion correlation interactions with temperature. The constraint is that the absolute value of the surface charge density of the colloids must be above a certain threshold, i.e., high enough such that the attractive ion−ion correlations can dominate the interaction regarding the divalent ions. The current conclusions are supported by the microstructural characterization of Ca^{2+}/Na^{+}-montmorillonite clay using small-angle X-ray scattering. A qualitative agreement is observed between the simulations and the experimental data.

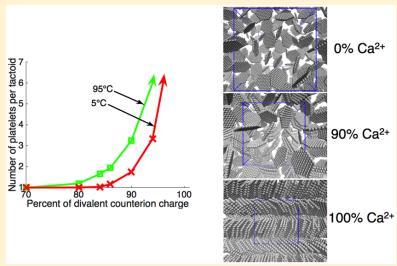

INTRODUCTION

When a charged colloid is dissolved in aqueous or polar solvents, the macromolecule becomes ionized, and there will be a release of counterions. Since macromolecules usually are highly charged, there will be counterions that confer enormous entropies of mixing. The counterions will form an electrical double layer, where the first layer is the surface charge of the macromolecule, and the second layer is composed of oppositely charged ions screening the first layer. Upon addition of multivalent ions to a system comprising monovalent counterions, there will be an ionic exchange in the double layer, and monovalent counterions will be released. With monovalent counterions in the system solely, the electrostatic interaction between the particles is repulsive, whereas when multivalent counterions are introduced, the interaction can be attractive due to the electrostatic ion−ion correlation effects. The latter is only valid under the constraint that the surface charge density is above a certain threshold.[1−8]

The above given mechanisms along with the charge distribution, the volume, the size, and the shape of the macromolecule, as well as the hydrophobic interactions, are the parameters that primarily determines the physicochemical properties of macromolecular solutions.

The model system of this study is montmorillonite, although we would like to emphasize that the obtained results are generally valid. Swelling 2:1 clay minerals consist of platelets with a thickness of about 1 nm and lateral dimensions varying from 25 nm in synthetic Laponite clays up to 1000 nm in natural montmorillonite. When water is added, the clay platelets become ionized, and the rising osmotic pressure in the solution causes the clay to swell.[9−11] Depending on the size, the platelets can form a lamellar structure, making it a seemingly perfect model system for an electrical double layer, where the swelling and the stability in saline solution depend strongly on the counterion valency and the surface charge density.[12−14] The situation is however, from a structural point, slightly less ideal. Clay is normally not a homogeneous lamellar material; it might better be described as a disordered structure of stacks of platelets, also denoted tactoids.[15−17]

Experimentally[18] and theoretically,[19] it has been found that for mixtures of Ca^{2+}/Na^{+}-montmorillonite (with ∼20% sodium or more) the clay is behaving qualitatively as Na^{+}-montmorillonite. Recently, it has also been shown that the swelling pressure of the clay mineral in aqueous solution, as a function of temperature, can be understood from electrostatic ion−ion correlation interactions.[20] In an aqueous clay dispersion dominated by monovalent counterions, the swelling pressure increases with temperature due to entropic reasons, whereas in a clay with predominantly divalent counterions, the opposite behavior was found. The explanation is that the ion−ion correlations increase with temperature since the product $\epsilon_r T$ decreases, i.e., the dielectric permittivity multiplied with temperature. The latter is an effect of the fact that ϵ_r drops when T increases. The aim of this study is to investigate the

Received: January 27, 2017
Revised: March 15, 2017
Published: March 16, 2017

DOI: 10.1021/acs.jpcc.7b00882
J. Phys. Chem. C 2017, 121, 7951−7958

possibility to control the osmotic pressure response with temperature of charged colloidal particles by varying the ratio of monovalent/divalent counterions in the system.

For this purpose a coarse-grained model has been used, and the simulations assume that the solvent can be represented as an uniform temperature-dependent dielectric permittivity. The limitations of the model are that: (i) it does not explain the extralamellar swelling[19] that is found for homoionic Ca^{2+}-montmorillonite nor, (ii) the reverse swelling pressure trend with temperature for Na^{+}-montmorillonite, i.e., when the average distance between the platelets is smaller than 1 nm. The former is to the authors knowledge not well understood, and the latter is due to the fact that the water is represented by the dielectric permittivity of bulk water.[20,21] The theoretical predictions are verified by small-angle X-ray scattering (SAXS) data, and a good qualitative correspondence is achieved.

MATERIALS AND METHODS

Experimental Details. *Material and Sample Preparation.* In this study, Wyoming Bentonite (MX-80), which consists mainly of the swelling clay mineral sodium montmorillonite, has been used. Sodium saturated montmorillonite from MX-80 has the chemical formula:[22]

$$(Al_{3.1}Mg_{0.49}Fe_{0.38}Ti_{0.01})(Si_{7.89}Al_{0.11})O_{20}(OH)_4,\ 0.65Na^{+} \quad (1)$$

The thickness and the average lateral size of the montmorillonite platelets are approximately 1 and 250 nm, respectively.[23] The purification and ion exchange procedures for MX-80 are described elsewhere.[24] Analytical grade sodium chloride (purity, 99.5%) and calcium chloride (purity, 99.5%) were purchased from MERCK. The purified Na^{+}- and Ca^{2+}-montmorillonite were dried at 105 °C overnight and milled into a fine powder. The clay powder from respective clay were mixed in different proportions to obtain different fractions of calcium (divalent) counterion charge that is neutralizing the clay:

$$\eta_{Di} = \frac{m_{Ca-clay}}{m_{Ca-clay} + m_{Na-clay}} \approx \frac{2N_{Di}}{2N_{Di} + N_{Mon}} \quad (2)$$

where $m_{Ca-clay}$ is the mass of Ca^{2+}-montmorillonite and $m_{Na-clay}$ is the mass of the Na^{+}-montmorillonite, whereas N_{Mon} and N_{Di} are the number of monovalent and divalent counterions, respectively. An excess of Millipore water was added to the mixed clay powder such that the counterions could diffuse and equilibrate within the sample for 24 h. All the Ca^{2+}/Na^{+}-montmorillonite mixtures were dried at 105 °C overnight and milled into a fine powder. Finally, Millipore water was added to each mixture in order to obtain a water mass ratio equal to six, and the samples were set to equilibrate for one month. $w = 6$ corresponds to a clay volume fraction $\phi_c \approx D_w/(D_c w + D_w) = 6\%$, where $D_c = 2750$ kg/m^3 is the density of the clay[18] and $D_w = 1000$ kg/m^3 is the density of water.

SAXS. SAXS experiments were performed at beamline ID02 at the European Synchotron Radiation Facility (ESRF) in Grenoble, France.[25] The q-range in the measurements was $0.2 < q < 4.5$ nm^{-1}, where $q = 4\pi \sin(\theta)/\lambda$, 2θ is the scattering angle, and $\lambda = 0.1$ nm is the monochromatic beam wavelength. The detector was a 2D CCD Raynomix MX 170 HS with binning 4 × 4. For data reduction, the software SAXSutilities[26] was used. The montmorillonite samples were measured in 1 mm sealed glass capillaries, and the background scattering (water) was subtracted. SAXS measurements were collected at different temperatures: 5, 25, 55, and 90 °C. The thermalization time of each temperature was 12 min.

In order to estimate the size of the aggregates, i.e., the average number of clay platelets per aggregate, a model scattering peak has been fitted to the experimental data. The scattering function was approximated with a Lorentzian line shape:

$$q^2 I(q) \propto \frac{w}{(q - q_{max})^2 + w^2} + b \quad (3)$$

where $I(q)$ is the scattering intensity, b is a fitting parameter for the background contribution, and w is a measure of the width. The full width at half-maximum (fwhm) of the peak is equal to $2w$, and the average tactoid size can be expressed as $\langle N \rangle \approx q_{max}/w$.[24,27,28] The data was fitted between $q_{max} \pm 0.5$ nm^{-1}, in order to make the peak fitting procedure as reasonable as possible.

Model and Simulations. *Bulk Simulations.* The interaction potentials and the platelet description are given elsewhere.[29] The electrostatic potential between particle i and j is defined as:

$$\beta u_{ij}^{EL}(r_{ij}, T) = \frac{l_B z_i z_j}{r_{ij}} \quad (4)$$

where $\beta = 1/(k_B T)$, k_B is the Boltzmann constant, $l_B = e^2/(4\pi\epsilon_0\epsilon_r(T)k_B T)$ is the Bjerrum length, e is the elementary unit charge, ϵ_0 is the permittivity of vacuum, z_i is the valency of particle i, and r_{ij} is distance between the particles. The solvent, i.e. the water molecules, is treated as a temperature-dependent, T, uniform dielectric permittivity, $\epsilon_r(T)$, with experimentally measured values of the dielectric permittivity of water.[30] The electrostatic interactions are enhanced as a function of temperature; i.e., the Bjerrum length increases as shown in Table 1. A truncated and shifted Lennard-Jones (TLJ) potential

Table 1. Bjerrum Length as a Function of Temperature[a]

T (°C)	T (K)	$\epsilon_r(T)$	l_B (nm)
5	278.15	85.76	0.700
25	298.15	78.30	0.716
95	368.15	57.01	0.796

[a]The Bjerrum length, l_B, at three different temperatures, T, and given dielectric permittivity, $\epsilon_r(T)$.[30]

has been used to represent the excluded volume of all particles in the system and is defined as:

$$u_{ij}^{TLJ}(r_{ij}) = \begin{cases} \epsilon\left[\left(\frac{\sigma_{ij}}{r_{ij}}\right)^{12} - 2\left(\frac{\sigma_{ij}}{r_{ij}}\right)^{6} + 1\right] & \text{if } r_{ij} \geq \sigma_{ij} \\ 0 & \text{otherwise} \end{cases} \quad (5)$$

where $\sigma_{ij} = (\sigma_i + \sigma_j)/2$, $\sigma_{ion} = 4$ Å, and $\sigma_{site} = 10$ Å. This potential has been chosen to be temperature independent and the strength of the short-ranged potential was set to $\epsilon = k_B \cdot 298$ J. Hence, the distribution of uncharged particles behaves independently of the temperature, with the aim to study the electrostatic effects solely.

The bulk molecular dynamics (MD) simulations were performed with the software package GROMACS (version 5.0.4).[31] Fifty negatively charged platelets with their corre-

DOI: 10.1021/acs.jpcc.7b00882
J. Phys. Chem. C 2017, 121, 7951−7958

sponding counterions were placed into a cubic simulation box with three-dimensional periodic boundary conditions. The platelets consist of 91 connected charged sites, and the one-sided surface charge density $\sigma = -2.6$ e/nm^2.[29] The absolute value of the surface charge density is chosen much higher than that of montmorillonite due to the small size of the simulated platelets. If the simulated platelets would be larger, the surface charge density can be reduced to have similar probability of aggregation as the smaller ones with divalent counterions.[29] On average, montmorillonite has a one-sided surface charge density of -1.5 e/nm^2.[32]

Newton's equations of motion of the freely moving species (platelets + ions) were integrated using the leapfrog algorithm. The time step was chosen to be 10 fs and gave the same results as using 1 fs time step (data not shown). The pressure was set by isotropic Berendsen pressure coupling for the NPT simulations, and the temperature was set by velocity-rescaling temperature coupling. All simulations assume equilibrium with salt-free water, and hence, the pressure is equal to the osmotic pressure. To account for the long-ranged electrostatic interactions, fast particle-mesh Ewald summation (PME) was used with a 6 nm real-space Coulomb cutoff (the largest and smallest box length used in the simulations are 70 and 20 nm, respectively) and a Fourier spacing equal to 0.6 nm. Different starting configurations for the equilibration simulation were performed both from a dilute and a compressed system to confirm that the mean volume and mean energy converged to the same value. For an in-depth description of the input parameters, see the online user manual.[31]

The volume fraction is a function of temperature, T, and osmotic pressure, Π, and is defined as:

$$\phi(T, \Pi) = \frac{4\pi r^3 N_{\text{sites}}}{3V_s(T, \Pi)} \tag{6}$$

where $r = 0.5$ nm is the radius of a platelet site, N_{sites} is the number of connected charged sites per platelet, and $V_s(T,\Pi)$ is the volume per platelet.

Two Parallel Surfaces. Two infinite parallel surfaces with a specific surface charge density and its corresponding counterions were simulated using Monte Carlo (MC) simulations described elsewhere.[19] The surface charge is smeared out, and the ions are treated as charged hard spheres. The electrostatic interactions between two ions are defined similarly as in the bulk simulations. The counterions in the bulk simulations are free to explore the volume between the surfaces, whereas in the MC simulations it is assumed that the counterion ratio is constant. An alternative to this simplification is to use a variant of the grand canonical ensemble.[33] For a given separation between the surfaces, h, and temperature, the osmotic pressure, $\Pi = \Pi(T,h)$, can be calculated using a midplane approach[1] written as:

$$\Pi = \Pi^{\text{id}} + \Pi^{\text{corr}} + \Pi^{\text{coll}} \tag{7}$$

where $\Pi^{\text{id}} = k_B T \sum_{i=1}^{2} c_i(\text{mp})$ is the ideal contribution, $c_i(\text{mp})$ is the concentration of counterions at the midplane with valency i, Π^{corr} is an attractive term due to the ion−ion correlations on either side of the midplane, and Π^{coll} is the collision term due to the finite-sized ions. The osmotic pressure response with temperature is calculated between 25 and 95 °C:

$$\Delta\Pi = \Pi(T = 95\ ^\circ\text{C}, h_{\text{fix}}) - \Pi(T = 25\ ^\circ\text{C}, h_{\text{fix}}) \tag{8}$$

where h_{fix} is defined to be the separation where the osmotic pressure is 4 bar for 25 °C.

RESULTS AND DISCUSSION

NVT Bulk Simulations. Three radial distribution functions (rdfs) are shown with respect to the center-of-mass between the platelets from NVT bulk simulations in Figure 1a. The

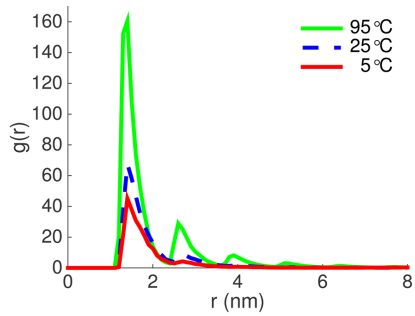

(a) Radial distribution functions for three different temperatures.

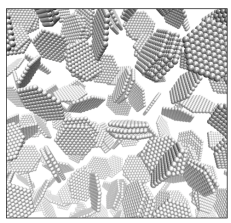

(b) T=5°C, ϵ_r=85.7

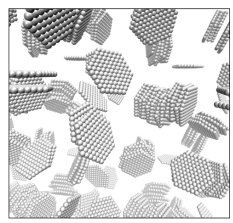

(c) T=95°C, ϵ_r=57.0

Figure 1. (a) Radial distribution functions between the platelets from NVT simulations at three different temperatures with $\eta_{\text{Di}} = 0.96$. (b, c) Representative configurations from the simulations for two temperatures. The counterions are omitted due to clarity, and the platelets are shown in gray.

volume of the platelets divided by the total volume is 4% (ϕ = 0.04), and $\eta_{\text{Di}} = 0.96$; i.e., 96% of the charge of the platelets are neutralized by divalent cations. The first peak at ∼1.3 nm corresponds to two platelets aggregated face-to-face. The height of the peak is related to the probability of finding that configuration. If three platelets have aggregated, a second peak arises at ∼1.3·2 = 2.6 nm. If four platelets have aggregated, a third peak arises at ∼1.3·3 = 3.9 nm and so on. Thus, the number of visible peaks in the rdfs gives an indication of the average number of platelets per tactoid, $\langle N \rangle$, and it can been seen that $\langle N \rangle$ increases with temperature. As the temperature is increasing from 5 to 95 °C, the attractive ion−ion correlations are enhanced[20] due to the ∼14% increase in Bjerrum length (see Table 1), which consequently leads to larger aggregates and a reduced osmotic pressure ($\langle N \rangle \sim 1.5$, $\Pi \sim 0.25$ bar at 5 °C, and $\langle N \rangle \sim 3.0$, $\Pi \sim 0.20$ bar at 95 °C). Typical configurations from the simulations are shown in Figure 1b,c, where it is displayed that larger aggregates are found at higher temperatures. Thus, for the particular surface charge density, volume fraction, and fraction of divalent counterions, we find:

DOI: 10.1021/acs.jpcc.7b00882
J. Phys. Chem. C 2017, 121, 7951−7958

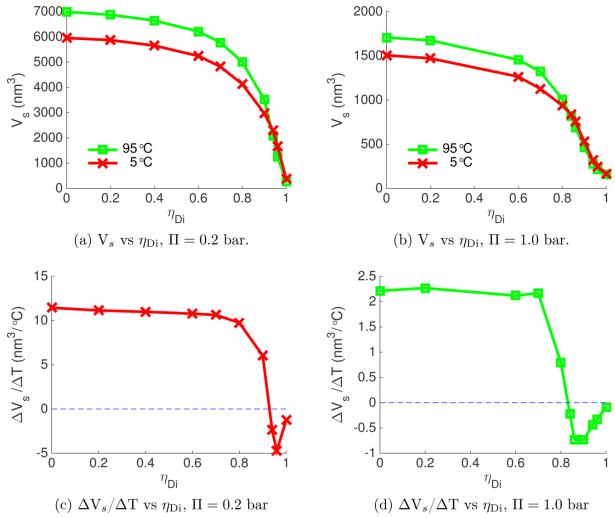

(a) V_s vs η_{Di}, $\Pi = 0.2$ bar. (b) V_s vs η_{Di}, $\Pi = 1.0$ bar.

(c) $\Delta V_s/\Delta T$ vs η_{Di}, $\Pi = 0.2$ bar (d) $\Delta V_s/\Delta T$ vs η_{Di}, $\Pi = 1.0$ bar

Figure 2. (a, b) Volume per platelet as a function of the fraction of charges that is neutralized by divalent counterions. (c, d) Difference in volume per platelet between 5 and 95 °C divided by the temperature difference as a function of η_{Di}. For 1 bar the crossover is found at $\eta_{Di} \sim 0.8$. That is, the volume per platelet is increased below $\eta_{Di} \sim 0.8$ and reduced above $\eta_{Di} \sim 0.8$ when the temperature is increased. For $\Pi = 0.2$ bar the crossover is found at $\eta_{Di} \sim 0.9$. Because of counterion dilution at lower pressures, the crossover occurs at higher divalent content.

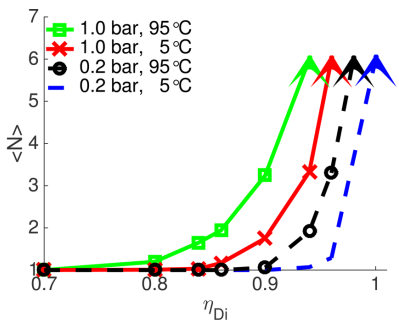

(a) $\langle N \rangle$ vs η_{Di}

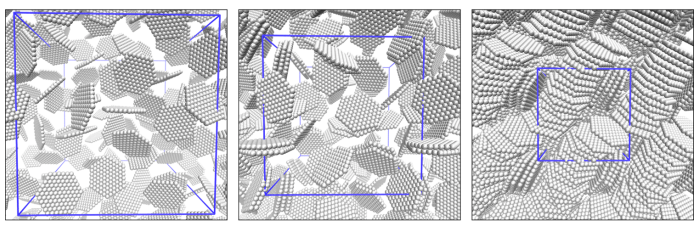

(b) $\eta_{Di} = 0$ (c) $\eta_{Di} = 0.84$ (d) $\eta_{Di} = 1.0$

Figure 3. (a) The average number of platelets per tactoid, $\langle N \rangle$, as a function of η_{Di} for 0.2 and 1.0 bar, respectively. The aggregation is initiated at lower fractions of divalent counterions when the temperature and/or pressure are increased. (b–d) Three configurations from the simulations for $T = 95$ °C, $\Pi = 1$ bar at different η_{Di}. The counterions are omitted due to clarity, the platelets are shown in gray, and the cubic simulation box is shown in blue (periodic images are shown outside the simulation box).

DOI: 10.1021/acs.jpcc.7b00882
J. Phys. Chem. C 2017, 121, 7951−7958

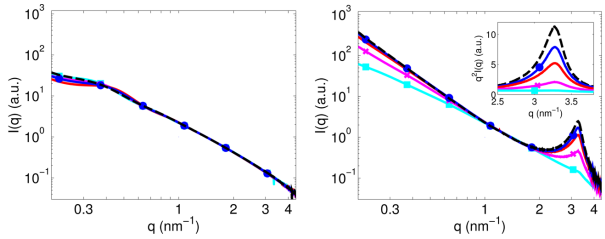

(a) η_{Di} =0, 0.05, 0.1, 0.2, and 0.4 at T=25°C (b) η_{Di} =0.6, 0.8, 0.9, 0.95, and 1.0 at T=25°C

Figure 4. X-ray scattering intensities as a function of the scattering vector at T = 25 °C of the Ca^{2+}/Na^{+}-montmorillonite fractions with ϕ = 0.06 for (a) η_{Di} = 0 (cyan square), 0.05 (magenta cross), 0.1 (red line), 0.2 (blue circle), and 0.4 (black dashed) and, (b) η_{Di} = 0.6 (cyan square), 0.8 (magenta cross), 0.9 (red line), 0.95 (blue circle), and 1.0 (black dashed). The inset in (b) shows the Kratky plots over a narrow q-range. The scattering intensities are normalized at $q \approx 1$ nm^{-1}.

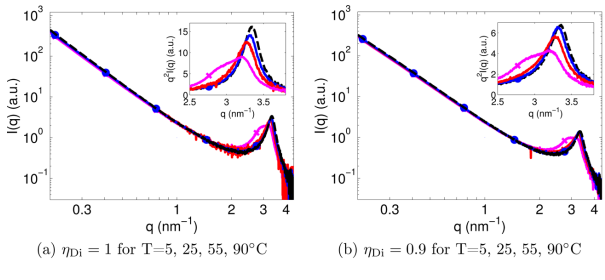

(a) η_{Di} = 1 for T=5, 25, 55, 90°C (b) η_{Di} = 0.9 for T=5, 25, 55, 90°C

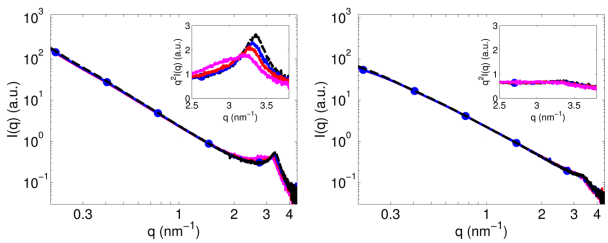

(c) η_{Di} = 0.8 for T=5, 25, 55, 90°C (d) η_{Di} = 0.6 for T=5, 25, 55, 90°C

Figure 5. X-ray scattering intensities as a function of the scattering vector for the temperature measurements of the Ca^{2+}/Na^{+}-montmorillonite fractions with ϕ = 0.06 for (a) η_{Di} = 1, (b) η_{Di} = 0.9, (c) η_{Di} = 0.8, and (d) η_{Di} = 0.6. The temperatures were 5 °C (magneta cross), 25 °C (red line), 55 °C (blue circle), and 90 °C (black dashed). The inset shows the Kratky plot over a narrow q-range.The scattering intensities are normalized at $q \approx 1$ nm^{-1}.

$$\Delta\Pi/\Delta T = \frac{\Pi(T = 95°C) - \Pi(T = 5°C)}{95°C - 5°C} \approx -60 \text{ Pa/°C}$$

which is in disagreement with the DLVO theory[34,35] that predicts $\Delta\Pi/\Delta T > 0$ for both monovalent and divalent counterions. With monovalent counterions and/or low enough surface charge density of the colloids, the DLVO theory predicts the correct trend as will be shown below.

NPT Bulk Simulations. In Figure 2a,b the volume per platelet as a function of fraction of divalent counterions can be seen for two different temperatures at two different pressures, 0.2 and 1.0 bar. At a low fraction of divalent counterions, the entropic repulsion dominates the system and the particles prefer to be far apart, which is clearly indicated by the large volume per platelet. At a high enough fraction of divalent counterions ($\eta_{Di} \sim 0.8$ for Π = 1.0 bar and $\eta_{Di} \sim 0.9$ for Π = 0.2 bar), the volume per platelet is decreasing rapidly, and the colloids tend to aggregate. In Figure 2c,d, the difference in volume per platelet divided by the temperature difference is shown as a function of the fraction divalent counterion charge. A crossover can be found where $\Delta V_s/\Delta T$ changes sign from positive to negative ($\eta_{Di} \sim 0.8$ for 1.0 bar and $\eta_{Di} \sim 0.9$ for 0.2 bar), and hence the conclusion is that $\Delta V_s/\Delta T$ can be chosen to be positive, negative, or kept constant by mixing counterions of different valency. Note that the volume response with temperature, $\Delta V_s/\Delta T$, in the NPT simulations is analogous to the osmotic pressure response, $\Delta\Pi/\Delta T$, in the NVT simulations. A minimum is found in the vicinity of the

DOI: 10.1021/acs.jpcc.7b00882
J. Phys. Chem. C 2017, 121, 7951−7958

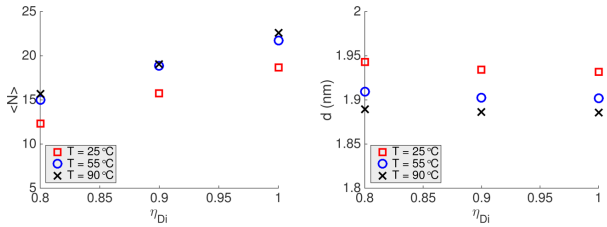

(a) $\langle N \rangle$ vs η_{Di} for T=25, 55, 90°C (b) d vs η_{Di} for T=25, 55, 90°C

Figure 6. (a) Average number of platelets per tactoid, $\langle N \rangle$, and (b) the average distance between the platelets as a function of the fraction divalent charges neutralizing the colloids, η_{Di}, obtained from the temperature measurements performed with SAXS for the Ca^{2+}/Na^{+}-montmorillonite fractions with ϕ = 0.06.

crossover where there are three effects that decreases the volume as the fraction of divalent counterions increases: (i) the single platelets form tactoids, (ii) the tactoids grow in size, and (iii) the separation between the platelets in a tactoid decreases. With 100% divalent counterions, all tactoids have aggregated at Π = 1 bar (see Figure 3d), and the change is due to to effect (iii) solely. The microstructure of the colloids is analyzed in Figure 3, where the average tactoid size is shown as a function of fraction of divalent counterions. As η_{Di} increases, the distance between single platelets decreases slightly (Figure 3b), and at the crossover the platelets start to aggregate into doublets and triplets (Figure 3c). The tactoids continue to grow in size, and finally, for a high enough fraction of divalent counterions and pressure (η_{Di} > 0.95 for Π = 1 bar), all tactoids have aggregated (Figure 3d). It should be emphasized that for $\langle N \rangle$ > 6 (indicated by the arrows) the average tactoid size cannot be calculated due to the limited size of the system, i.e., 50 platelets. The tactoid size for aggregated platelets has previously been investigated for parallel platelets with MC simulations,[32] and aggregates of spherical particles have been investigated with MC/MD simulations.[36]

SAXS. Scattering experiments were performed for the corresponding Ca^{2+}/Na^{+}-montmorillonite mixtures used in the bulk MD simulations. The scattering intensities for all mixtures at T = 25 °C and ϕ_c = 0.06 are shown in Figure 4. Bragg peaks are clearly observed for η_{Di} = 1, 0.95, 0.9, and 0.8 (Figure 4b), indicating that there are tactoids in these samples. Moreover, the fwhm of the Bragg peak is decreasing, which indicates that the tactoids are growing in size (see Figure 6a) as η_{Di} approaches one. For $\eta_{Di} \leq 0.6$ (Figure 4a), all the scattering intensity curves are qualitatively equal, and no Bragg peaks are visible, indicating that the systems are dominated by repulsive interactions. Hence, the SAXS measurements are in qualitative agreement with the simulations in Figure 3 and also agree well with the study by Hedström et al.,[18] i.e., Ca^{2+}/Na^{+}-montmorillonite with ~20% sodium or more, behaves qualitatively as a Na^{+}-montmorillonite, whereas montmorillonite with 90% or more calcium in the interlayer behaves similar to homoionic Ca^{2+}-montmorillonite.

The scattering intensities and the Kratky plots for η_{Di} = 1, 0.9, 0.8, and 0.6 with ϕ_c = 0.06 at four different temperatures, 5, 25, 55, and 90 °C, are shown in Figure 5. The positions of the Bragg peaks for η_{Di} = 1, 0.9, and 0.8 shift toward higher q-values as the temperature increases, as shown in Figure 5a–c. For η_{Di} = 0.6 no Bragg peak is visible, indicating that there are no tactoids in the system for any of the temperatures investigated (see Figure 5d). By comparing the value of $\langle N \rangle$ for the three different temperatures (T = 25 °C, T = 55 °C, and T = 90 °C), it is found that there is only a small difference between 55 and 90 °C. A larger deviation is found for 25 °C, which can be associated with changes in the microstructure of the system. The shift toward higher q-values in the Bragg peak with temperature indicates that the average distance between the platelets decreases with an increase in temperature, from ~1.93 to 1.89 nm, i.e., three water layers, for T = 25–90 °C (see Figure 6b). At 5 °C, the SAXS data seems to be composed by a superposition of two Bragg peaks, with an average distance of ~1.9–2.1 nm, corresponding to a combination of three and four water layers. These results are in agreement with the previous work done by Svensson and Hansen.[37,38]

The two trends where: (i) the spacing between the platelets in the tactoids is reducing, and (ii) the increase in number of platelets per tactoid with temperature for $\eta_{Di} \geq 0.8$, are found both in the simulations as well as in the experiments. Obviously, the model cannot find discrete distances between the platelets, such as three or four water layers, since the water molecules are represented as a uniform dielectric permittivity. Hence, a quantitative agreement at 5 °C is not possible.

Crossover for Two Parallel Surfaces. The platelets in the bulk simulations above have a fixed surface charge density, and the crossover from positive to negative change in pressure with temperature was found to be at approximately 90% and 80% divalent counterions, for 0.2 and 1 bar, respectively (Figure 2a,b). In Figure 7 the crossover between two parallel surfaces for $\Pi(T$ = 25 °C) = 4 bar (eq 8) has been simulated (MC

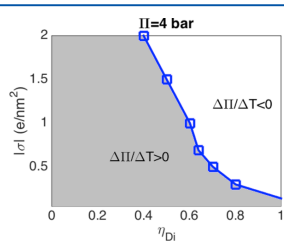

Figure 7. Crossover from increasing to decreasing osmotic pressure response with temperature is shown as a function of the surface charge density and the percentage of divalent counterions neutralizing the colloids. The osmotic pressure is 4 bar, and the temperature is 25 °C. The areas left/right of the line correspond to an increased/decreased osmotic pressure with increasing temperature.

DOI: 10.1021/acs.jpcc.7b00882
J. Phys. Chem. C 2017, 121, 7951–7958

simulations) for different absolute values of the surface charge density ranging from 0.05 to 2 e/nm^2. The pressure was chosen high enough to avoid any two-phase coexistence with opposite sign of $\Delta\Pi/\Delta T$. Furthermore, the crossover of the two parallel surfaces differs from the bulk simulations due to the exclusion of the rotational entropy, and the difference in electrostatic interaction between a small colloid and an infinite surface. The dark gray area on the left-hand side of the crossover-line corresponds to an increasing osmotic pressure with temperature, and the area on the right-hand side of the crossover-line corresponds to a decreasing osmotic pressure with temperature, as indicated in Figure 7. If $|\sigma| < 0.2$ e/nm^2, the DLVO theory is valid, even with 100% divalent counterions. As the surface charge density increases, a crossover appears, and it shifts toward a lower percentage of divalent counterions with an increased surface charge density. The latter is due to the fact that the attractive ion−ion correlations increase with increasing surface charge density.[6,32]

Finally, we would like to emphasize that the midplane approach is useful for understanding the importance of the different contributions to the pressure defined in eqs 7 and 8 as well as for understanding the limitations of the DLVO theory where the correlation term is neglected. In Table 2, it is shown

Table 2. Osmotic Pressure Response from the MC Simulations[a]

η_{Di}	h_{fix} (nm)	$\Delta\Pi^{id}$	$\Delta\Pi^{corr}$	$\Delta\Pi$
0.6	2.6	0.69	−0.43	0.26
0.7	2.1	1.00	−0.96	0.04
0.8	1.5	2.30	−3.50	−1.20

[a]The osmotic pressure response, $\Delta\Pi = \Delta\Pi^{id} + \Delta\Pi^{corr} + \Delta\Pi^{coll}$, between 25 and 95 °C, and the main components, $\Delta\Pi^{id}$ and $\Delta\Pi^{corr}$, are shown for $|\sigma| = 0.5$ e/nm^2 where the osmotic pressure is 4 bar at 25 °C.

that the difference in the ideal contribution, $\Delta\Pi^{id}$, is found to increase with the fraction of divalent counterions mainly due to the reduced separation. Although, by taking into account the difference in the correlation contribution, $\Delta\Pi^{corr}$, it is found that $\Delta\Pi/\Delta T < 0$ for $\eta_{Di} > 0.7$. Hence, the osmotic pressure response can be negative if the correlation difference is the leading term. The contribution $\Delta\Pi^{coll}$ is negligible and not shown.

CONCLUSIONS

We have shown that the electrostatic interactions alone can give a positive, negative, or constant osmotic pressure response with temperature, depending on the monovalent/divalent counterion ratio, if $|\sigma| > 0.2$ e/nm^2. The fraction of divalent counterions, where a crossover from positive to negative pressure response with temperature is found, depends on the surface charge density, the pressure (or volume fraction), and other components such as the rotational entropy and the size of the colloid. Mixtures of Ca^{2+}-montmorillonite and Na^{+}-montmorillonite in water were measured with SAXS at four different temperatures. It was found that Bragg peaks appear for a sodium content of ∼20% or less, which indicates that tactoids exist in those compositions. As the sodium content was reduced, the number of platelets per tactoid increased. By increasing the temperature, the separation between the platelets in the tactoids decreased and the number of platelets per tactoid seems to increase slightly. For a sodium content of ∼40% or more, no tactoids were found, which indicates that the interaction between the platelets are dominated by repulsive interactions. Our theoretical predictions are in good agreement with the SAXS experiments, giving a further indication that our model can explain the underlying physics. The theory presented here is general and predicts that the temperature response for all types of charged colloids can be controlled by mixing counterions of different valency if the interactions in the system are dominated by electrostatics. Even though the applied model is very simple, and only face charges are taken into consideration, we still believe that this study shed light on the fundamental physics of these systems, the formation of tactoids, and role of electrostatic interactions.

AUTHOR INFORMATION

Corresponding Authors

*E-mail: axel.thuresson@teokem.lu.se (A.T.).
*E-mail: marie.skepo@teokem.lu.se (M.S.).

ORCID

Axel Thuresson: 0000-0001-8459-1394

Notes

The authors declare no competing financial interest.

ACKNOWLEDGMENTS

Computational resources were provided by the Swedish National Infrastructure for Computing (SNIC) through Lunarc, the Center for Scientific and Technical Computing at Lund University. We acknowledge Dr. T. Narayanan and Dr. J. Möller for providing assistance during measurements at ESRF. The work was performed within the framework of the Swedish national strategic e-science research program eSSENCE. The Lars Hierta Memorial Foundation is greatly acknowledged for financial support.

REFERENCES

(1) Guldbrand, L.; Jönsson, B.; Wennerström, H.; Linse, P. Electric double layer forces. A Monte Carlo study. *J. Chem. Phys.* **1984**, *80*, 2221−2228.
(2) Guldbrand, L.; Nilsson, L.; Nordenskiöld, L. A Monte Carlo simulation study of electrostatic forces between hexagonally packed DNA double helices. *J. Chem. Phys.* **1986**, *85*, 6686−6698.
(3) Attard, P.; Kjellander, R.; Mitchell, D. J.; Jönsson, B. Electrostatic fluctuation interactions between neutral surfaces with adsorbed, mobile ions or dipoles. *J. Chem. Phys.* **1988**, *89*, 1664−1680.
(4) Kjellander, R.; Marčelja, S. Inhomogeneous Coulomb fluids with image interactions between planar surfaces. I. *J. Chem. Phys.* **1985**, *82*, 2122−2135.
(5) Kjellander, R.; Marčelja, S.; Pashley, R. M.; Quirk, J. P. Double-layer ion correlation forces restrict Calcium clay swelling. *J. Phys. Chem.* **1988**, *92*, 6489−6492.
(6) Pellenq, R. J.-M.; Caillol, J. M.; Delville, A. Electrostatic attraction between two charged surfaces: A (N,V,T) Monte Carlo simulation. *J. Phys. Chem. B* **1997**, *101*, 8584−8594.
(7) Netz, R. Electrostatistics of counter-ions at and between planar charged walls: From Poisson-Boltzmann to the strong-coupling theory. *Eur. Phys. J. E: Soft Matter Biol. Phys.* **2001**, *5*, 557−574.
(8) Jönsson, B.; Nonat, A.; Labbez, C.; Cabane, B.; Wennerström, H. Controlling the cohesion of cement paste. *Langmuir* **2005**, *21*, 9211−9221.
(9) Mongondry, P.; Tassin, J. F. T.; Nicolai, T. Revised state diagram of Laponite dispersions. *J. Colloid Interface Sci.* **2005**, *283*, 397−405.
(10) Mourchid, A.; Lécolier, E.; Van Damme, H.; Levitz, P. On viscoelastic, birefringent, and swelling properties of Laponite clay suspensions: Revisited phase diagram. *Langmuir* **1998**, *14*, 4718−4723.

DOI: 10.1021/acs.jpcc.7b00882
J. Phys. Chem. C 2017, 121, 7951−7958

(11) Pignon, F.; Magnin, A.; Piau, J.-M.; Cabane, B.; Lindner, P.; Diat, O. Yield stress thixotropic clay suspension: Investigations of structure by light, neutron, and X-ray scattering. *Phys. Rev. E: Stat. Phys., Plasmas, Fluids, Relat. Interdiscip. Top.* **1997**, *56*, 3281.
(12) Blackmore, A. V.; Warkentin, B. P. Swelling of calcium montmorillonite. *Nature* **1960**, *186*, 823−824.
(13) Jönsson, B.; Wennerström, H. *Electrostatic Effects in Soft Matter and Biophysics*; Springer: Netherlands, 2001; pp 171−204.
(14) Karnland, O.; Olsson, S.; Nilsson, U.; Sellin, P. Experimentally determined swelling pressures and geochemical interactions of compacted Wyoming bentonite with highly alkaline solutions. *Phys. Chem. Earth, Parts A/B/C* **2007**, *32*, 275−286.
(15) Banin, A. Tactoid formation in montmorillionite: effect on ion exchange kinetics. *Science* **1967**, *155*, 71−72.
(16) Meunier, A. *Clays*; Springer Science & Business Media: 2005.
(17) Shalkevich, A.; Stradner, A.; Bhat, S. K.; Muller, F.; Schurtenberger, P. Cluster, glass, and gel formation and viscoelastic phase separation in aqueous clay suspensions. *Langmuir* **2007**, *23*, 3570−3580.
(18) Hedström, M.; Birgersson, M.; Nilsson, U.; Karnland, O. Role of cation mixing in the sol formation of Ca/Na-montmorillonite. *Phys. Chem. Earth, PT A/B/C* **2011**, *36*, 1564−1571.
(19) Segad, M.; Jönsson, B.; Åkesson, T.; Cabane, B. Ca/Na montmorillonite: Structure, forces and swelling properties. *Langmuir* **2010**, *26*, 5782−5790.
(20) Thuresson, A.; Karnland, O.; Jönsson, B. Anomalous temperature behavior in clay swelling due to ion-ion correlations. *EPL* **2016**, *114*, 38002.
(21) Birgersson, M.; Karnland, O.; Nilsson, U. Freezing of bentonite. Experimental studies and theoretical considerations. SKB Technical Report, 2010; TR-10-40, 1-1.
(22) Karnland, O.; Olsson, S.; Nilsson, U. Mineralogy and sealing properties of various bentonites and smectite-rich clay materials. SKB Technical Report, 2006; TR-06-30, 1-1.
(23) Michot, L. J.; Bihannic, I.; Porsch, K.; Maddi, S.; Baravian, C.; Mougel, J.; Levitz, P. Phase diagrams of Wyoming Na-montmorillonite clay. Influence of particle anisotropy. *Langmuir* **2004**, *20*, 10829−10837.
(24) Segad, M.; Jönsson, B.; Cabane, B. Tactoid formation in montmorillonite. *J. Phys. Chem. C* **2012**, *116*, 25425−25433.
(25) van Vaerenbergh, P.; Léonardon, J.; Sztucki, M.; Boesecke, P.; Gorini, J.; Claustre, L.; Sever, F.; Morse, J.; Narayanan, T. An upgrade beamline for combined wide, and ultra and ultra -angle X-ray scattering at the ESRF. *AIP Conf. Proc.* **2015**, *1741*, 030034.
(26) Sztucki, M. (2011) SAXSutilities download page: http://www.sztucki.de/SAXSutilities, (accessed Mar 2017).
(27) Segad, M.; Hanski, S.; Olsson, U.; Ruokolainen, J.; Åkesson, T.; Jönsson, B. Microstructural and swelling properties of Ca and Na montmorillonite: (In situ) Observations with Cryo-TEM and SAXS. *J. Phys. Chem. C* **2012**, *116*, 7596−7601.
(28) Segad, M. Microstructure determination of IQ-WB clays: a direct procedure by small-angle X-ray scattering. *J. Appl. Crystallogr.* **2013**, *46*, 1316−1322.
(29) Thuresson, A.; Ullner, M.; Turesson, M. Interaction and aggregation of charged platelets in electrolyte solutions: A coarse-graining approach. *J. Phys. Chem. B* **2014**, *118*, 7405−7413.
(30) Malmberg, C. G.; Maryott, A. A. Dielectric constant of water from 0° to 100° C. *J. Res. Nat. Bureau Stand* **1956**, *56*, 1−8.
(31) Abraham, M.; van der Spoel, D.; Lindahl, E.; Hess, B. the GROMACS development team, GROMACS User Manual version 5.0.1, 2014.
(32) Thuresson, A.; Ullner, M.; Åkesson, T.; Labbez, C.; Jönsson, B. Monte Carlo simulations of parallel charged platelets as an approach to tactoid formation in clay. *Langmuir* **2013**, *29*, 9216−9223.
(33) Turesson, M.; Forsman, J.; Åkesson, T.; Jönsson, B. Simulation of phase equilibria in lamellar surfactant systems. *Langmuir* **2004**, *20*, 5123−5126.
(34) Derjaguin, B. V.; Landau, L. Theory of the stability of strongly charged lyophobic sols and of the adhesion of strongly charged particles in solutions of electrolytes. *Acta Phys. Chim. URSS* **1941**, *14*, 633−662.
(35) Verwey, E. J. W.; Overbeek, J. T. G. *Theory of the Stability of Lyophobic Colloids*; Elsevier Publishing Company Inc.: Amsterdam, 1948.
(36) Linse, P.; Lobaskin, V. Electrostatic attraction and phase separation in solutions of like-charged colloidal particles. *J. Chem. Phys.* **2000**, *112*, 3917−3927.
(37) Svensson, P. D.; Hansen, S. Combined salt and temperature impact on montmorillonite hydration. *Clays Clay Miner.* **2013**, *61*, 328−341.
(38) Svensson, P. D. Ph.D. Thesis, Lund University, Lund, Sweden, 2015.

DOI: 10.1021/acs.jpcc.7b00882
J. Phys. Chem. C 2017, 121, 7951−7958

Paper II

Reprinted from *J. Colloid Interface Sci.*, **513**
M. Jansson, A. Thuresson, T. S. Plivelic, J. Forsman, and M. Skepö
The Effect of the Relative Permittivity on the Tactoid Formation in Nanoplatelet Systems. A Combined Computer Simulation, SAXS, and Osmotic Pressure Study., 575-584, 2018

Journal of Colloid and Interface Science 513 (2018) 575–584

Contents lists available at ScienceDirect

Journal of Colloid and Interface Science

journal homepage: www.elsevier.com/locate/jcis

Regular Article

The effect of the relative permittivity on the tactoid formation in nanoplatelet systems. A combined computer simulation, SAXS, and osmotic pressure study

Maria Jansson [a,*], Axel Thuresson [a], Tomás S. Plivelic [b], Jan Forsman [a], Marie Skepö [a,*]

[a] Theoretical Chemistry, Lund University, P.O. Box 124, SE-221 00 Lund, Sweden
[b] MAX IV Laboratory, Lund University, P.O. Box 118, SE-221 00 Lund, Sweden

GRAPHICAL ABSTRACT

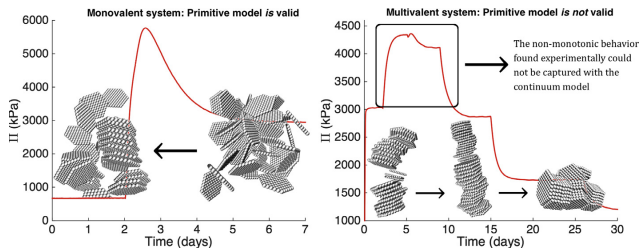

ARTICLE INFO

Article history:
Received 6 October 2017
Revised 14 November 2017
Accepted 16 November 2017
Available online 20 November 2017

Keywords:
Nanoplatelets
Clay
Montmorillonite
Molecular dynamics simulations
Monte Carlo simulations
Electrostatic interactions
Ion-ion correlations
Relative permittivity
Ethanol
Small angle X-ray scattering

ABSTRACT

The structural properties, and the intracrystalline swelling of Na^+-, and Ca^{2+}-montmorillonite (Na-, and Ca-mmt) have been investigated as an effect of decreasing the relative permittivity of the solvent, i.e. from water to ethanol (EtOH), utilizing the experimental techniques; small angle X-ray scattering (SAXS) and osmotic pressure measurements. The experimental data were compared with the continuum model, utilizing coarse-grained molecular dynamics bulk simulations, Monte Carlo simulations of two infinite parallel surfaces corresponding to two clay platelets, and the strong coupling theory. It was found that it is possible to tune the electrostatic interactions to obtain a transition from a repulsive to an attractive system for the Na-mmt by increasing the EtOH concentration, i.e. the Bjerrum length increases, and hence, the attractive ion-ion correlation forces are enhanced. A qualitative agreement was observed between the simulations and the experimental results. Moreover, a non-monotonic behavior of the intracrystalline swelling of Ca-mmt as a function of EtOH concentration was captured experimentally, where an increase in the osmotic pressure, and hence, an increase in the *d*-spacing was found at low concentrations, indicating that repulsive short-ranged interactions dominate in the system. Theoretically, the non-monotonic behavior could not be captured with the continuum model, probably due to the limitation that the electrostatic interactions solely enters the Hamiltonian via the Bjerrum length.

* Corresponding authors.
E-mail addresses: maria.jansson@teokem.lu.se (M. Jansson), marie.skepo@teokem.lu.se (M. Skepö).

https://doi.org/10.1016/j.jcis.2017.11.051
0021-9797/

1. Introduction

Clay is a complex colloidal system and refers to naturally occurring aluminosilicate layered minerals, denoted phyllosilicates. The clay platelet has a strong negative surface charge density compensated with interlayer exchangeable cations. The physiochemical properties, and also the colloidal behavior, are determined by the charge distribution, the volume, and the shape of the colloid. When dispersed in water, the clay platelet becomes ionized and a rising osmotic pressure in the solution causes the clay to swell [1,2]. Semi-dilute dispersions can behave as gels, i.e. they have the ability to form yield stress materials [3–5], which are comprehensively used in various industrial applications, such as in paint, in drilling fluids, and in food as well as in cosmetic industry. For this reason, clay-solvent interactions have been extensively studied by evaluating the intracrystalline swelling of montmorillonite (mmt) in water [6,7], in different organic solvents [8–10], as well as water/organic mixtures [11]. Theoretically, the understanding of the swelling behavior of Na^+-montmorillonite (Na-mmt) in water and ethanol (EtOH) have been studied by Metz et al. [9] utilizing atomistic computer simulations. They have found that the initial solvation of dry clay with EtOH is energetically unfavourable by comparing the solvation energetics with the energy of the bulk, and that the formation of an EtOH monolayer is associated with a large energy barrier to move the first EtOH molecules into the interlayer region. Moreover, they found that the Na^+ ions behave differently in EtOH compared to in water, where the density profiles showed that the ions aggregate at each clay surface in the former rather than being dispersed in the solvent. Experimentally, the intracrystalline swelling of Ca^{2+}-montmorillonite (Ca-mmt) in water/EtOH mixtures was studied by Brindley et al. [11] using X-ray diffractometry. In their study, they found that for Ca-mmt the equilibrium basal spacing increased to about 35 mol percent of EtOH, and beyond the maximum expansion, the d-spacing diminished abruptly. Their explanation of the initial increase in basal spacing is due to an increased repulsion arising from the replacement of water molecules by the larger EtOH molecules, i.e. an excluded volume effect. Moreover, Brindley et al. concluded that the initial increase is not compatible with the accompanying decrease of the relative permittivity, due to the fact that it would cause an increase in the attractive electrostatic forces. However, to the authors knowledge, both effects can be present in the system, where the increase in basal spacing can be explained through an intricate balance of the partitioning of the solvent molecules, the electrostatic repulsive forces, and the enhanced ion-ion correlation forces.

The aim of this work is to study how the structural properties of the tactoids, and the intracrystalline swelling, are affected by changing the solvent i.e. by decreasing the relative permittivity for Na-, and Ca-mmt in water/EtOH mixtures. The focus is on describing under which conditions the structural properties of Na-mmt behaves as Ca-mmt, i.e. the possibility to tune the electrostatic interactions to obtain a transition from a repulsive to an attractive clay system via the solvent properties. For this purpose the experimental techniques, *Small Angle X-ray Scattering* (SAXS) and osmotic pressure measurements have been used. The experimental data are compared with theoretical models, such as: coarse-grained molecular dynamics (MD) bulk simulations, Monte Carlo (MC) simulations of two infinite parallel surfaces corresponding to two clay platelets, and with strong coupling theory.

Our main findings are that when increasing the concentration of EtOH, the attractive ion-ion correlation forces are enhanced, concluding that the structural properties of Na-mmt do indeed behave similarly as Ca-mmt. This is confirmed both experimentally and theoretically, where the transition from a repulsive to an attractive system is found. For Ca-mmt, a non-monotonic behavior of the intracrystalline swelling as a function of EtOH concentration was found experimentally, where the distance between the platelets and the osmotic pressure increased at low concentrations of EtOH, indicating that repulsive short-ranged interactions are dominating in the system. This behavior could, however, not be captured theoretically, probably due to the limitation in the continuum model, i.e. that the solvent is represented by the relative permittivity of the bulk solvent.

2. Experimental section

2.1. Chemicals and materials

The type of natural clay used throughout this study was Wyoming bentonite (MX-80), which is mainly composed of the swelling clay mineral Na-mmt. The chemical formula for the sodium saturated montmorillonite from MX-80 can be written as [12]:

$$(Al_{3.1}Mg_{0.49}Fe_{0.38}Ti_{0.01})(Si_{7.89}Al_{0.11})O_{20}(OH)_4, 0.65Na^+. \quad (1)$$

The purification and ion exchange procedures for MX-80 are described elsewhere [13]. Analytical grade sodium chloride (purity, 99.5%), and calcium chloride (purity, 99.5%) were purchased from MERCK. The purified Na-mmt and Ca-mmt were dried in an oven at 105 °C over night, and milled into a fine powder. EtOH solutions were prepared by dilution of EtOH 95 wt% (analytical grade, SOLVECO) with millipore water. The Na-, and Ca-mmt powder were added to different water/EtOH solutions, respectively, in order to obtain a clay volume fraction of 6% ($\phi_c \approx 0.06$). After the sample preparations, the samples were left to equilibrate for one month.

2.2. Methods and instruments

SAXS experiments were performed at beamline ID02 at the European Synchotron Radiation Facility (ESRF) in Grenoble-France [14]. For data reduction, the software SAXS-utilities [15] was used. The q-range reported in this study is $6.1 \cdot 10^{-2} < q < 4.5\ \mathrm{nm}^{-1}$, where $q = 4\pi\sin(\theta)/\lambda, 2\theta$ is the scattering angle, and $\lambda = 0.1$ nm is the monochromatic beam wavelength. The detector was a 2D CCD Rayonix MX 170 HS with binning 4×4. SAXS measurements were collected at different water/EtOH solutions: 0, 20, 40, 60, and 95 wt% EtOH, and at two different temperatures, room temperature, and the other significantly higher, 27, and 63 °C, respectively, where the thermalization time of each temperature was 12 min. For accurate statistics, and to control possible radiation damage effects, an average over ten frames was collected for each sample. The liquid samples were measured in 1 mm sealed glass capillaries, and the solid sample was placed between two mica sheets in a customized sample holder [14]. The background scattering was subtracted, where the corresponding water/EtOH solution was used for the liquid samples, and one empty cell with two mica sheets for the solid samples.

In order to estimate the size of the aggregates, i.e. the average number of clay platelets per tactoid, a model scattering peak has been fitted to the experimental data. The scattering function can be approximated with a Lorentzian line shape:

$$q^2 I(q) \propto \frac{w}{(q - q_{max})^2 + w^2} + b, \quad (2)$$

where $I(q)$ is the scattering intensity, w is a measure of the width of the Bragg peak, q_{max} is the position of maximum intensity of the Bragg peak, and b is a fitting parameter for the background

Table 1
The Bjerrum length as a function of EtOH concentration and temperature.[a]

wt% EtOH	ϵ_r(T = 20 °C)	l_B (nm)	ϵ_r(T = 60 °C)	l_B (nm)
0	80.4	0.708	66.6	0.753
20	68.7	0.829	56.4	0.889
40	56.5	1.008	45.8	1.095
60	44.7	1.274	35.7	1.407
80	33.9	1.679	26.3	1.906
90	29.0	1.963	22.5	2.228
95	27.0	2.111	21.0	2.388
100	25.0	2.277	19.6	2.566

[a] The Bjerrum length, l_B, at eight different wt% of EtOH, and two temperatures, T, with corresponding relative permittivity, ϵ_r(T) [20].

contribution. The full width at half maximum (FWHM) of the peak is equal to $2w$, and the average tactoid size can be expressed as $\langle N\rangle \approx q_{max}/w$ [13,16,17]. The average distance, i.e. d-spacing, between the midplane of two adjacent clay platelets was obtained from q_{max} via the relation: $d_{Bragg} = 2\pi/q_{max}$. The data was fitted between $q_{max} \pm 0.5$ nm^{-1}.

To achieve an indication of how the solvent properties affect the intracrystalline swelling, the osmotic pressures of the clay systems were directly measured using a test cell [12,18]. Approximately one gram of clay was placed within the test cell and confined by a piston, which is attached to a force transducer. The Na-, and Ca-mmt were set to equilibrate with a successive replacement of different solvent compositions corresponding to 0, 20, 40, 60, 80, and 95 wt% EtOH, through a semipermeable membrane, which was permeable to the solvent, but not to the clay particles. For the solvent composition of 0 wt% EtOH, used for the Na-mmt, NaCl with a salt concentration above the critical coagulation concentration (CCC) was added, i.e. 50 mM NaCl, to prevent any leakage through the membrane. The resulting osmotic pressure was calculated from the recorded force and piston contact area. With this experimental technique it is difficult to prepare the test cell to give an exact final volume, and hence, two separate measurements are rarely identical. However, it is possible to accurately determine the clay water content after the measurement, and thus the clay system was set to equilibrate with 0 wt% EtOH in the final stage. The clay water content is defined as $w = m_w/m_s$, where m_w is the mass of the water, and m_s is the mass of the solid. From the clay water content, the dry density of the clay defined as $D_d = m_s/V$ can be determined, utilizing $D_d = D_w/(w + D_w/D_s)$, where V is the total volume of the system, D_s (2750 kg/m^3) and D_w (1000 kg/m^3) are the densities of the solid, and the water, respectively.

3. Theoretical section

3.1. Model and simulations

Molecular dynamics bulk simulations were used to study the structural and the thermodynamical properties of the formed tactoids of Na-mmt as a function of EtOH concentration, where the interaction potentials and the platelet description are given elsewhere [19]. The electrostatic (EL) pair-potential between particle i and j is defined as:

$$\beta u_{ij}^{\mathrm{EL}}(r,T) = \frac{l_B z_i z_j}{r_{ij}}, \tag{3}$$

where $\beta = 1/(k_B T)$, k_B is the Boltzmann constant, $l_B = e^2/(4\pi\epsilon_0\epsilon_r(T)k_B T)$ is the Bjerrum length, e is the elementary unit charge, ε_0 is the permittivity of vacuum, z_i is the valency of particle i, and r_{ij} is the center-to-center distance between the particles. The solvent is treated implicitly through the relative permittivity $\epsilon_r(T)$, and regarded as temperature (T) dependent. The solvent effect was studied by varying the value of $\epsilon_r(T)$ for the medium corresponding to experimentally measured values of the relative permittivity of water, EtOH, and water/EtOH mixtures, see Table 1 [20]. When increasing the EtOH concentration, the Bjerrum length increases, resulting in enhanced attractive ion-ion correlation forces due to an increased repulsion between the ions.

In addition to the electrostatic pair-potential, the particles also interact via a strictly repulsive, truncated, and shifted Lennard-Jones (LJ) potential, defined as:

$$u_{ij}^{\mathrm{LJ}}(r_{ij}) = \begin{cases} \epsilon_{\mathrm{LJ}}\left[\left(\frac{\sigma_{ij}}{r_{ij}}\right)^{12} - 2\left(\frac{\sigma_{ij}}{r_{ij}}\right)^{6} + 1\right], & \text{if } r_{ij} < \sigma_{ij} \\ 0, & \text{otherwise} \end{cases}, \tag{4}$$

where $\sigma_{ij} = (\sigma_i + \sigma_j)/2$, $\sigma_{ion} = 4$ Å, and $\sigma_{site} = 10$ Å. The strength of the short-ranged repulsion was set to $\epsilon_{LJ} = k_B \cdot 293$ J, with the motivation to obtain a temperature independent LJ potential. Thus, the distribution of uncharged particles behaves independently of the temperature, since the aim is to study the electrostatic effects exclusively.

The MD simulations were performed with the software package GROMACS (version 5.0.4.) [21]. The model consisted of 50 negatively charged finite plates, i.e. clay platelets, and their corresponding counterions in a cubic simulation box with three-dimensional periodic boundary conditions. The platelets had a hexagonal symmetry and were constructed from monolayers of 91 connected charged, truncated, and shifted LJ spheres, i.e. sites. The mean radius of the platelet was 5.5 nm, and the one-sided surface charge density was set to $\sigma = -2.6$ e/nm^2. Since the interaction is proportional to the area of the platelet, the absolute value of the surface charge density is chosen much higher than the estimated value of natural mmt to compensate for the small size of the simulated platelets. The reader should notice, that if the size of the simulated platelets would be larger, the surface charge density can be reduced to have similar probability of aggregation as the smaller platelets with divalent counterions [19]. Furthermore, the reason for this is that the interaction is to a first approximation proportional to the area of the platelets. On average, mmt has a one-sided surface charge density of -1.5 e/nm^2 [22].

Newton's equations of motion of freely moving species, i.e. the platelets and the counterions, were integrated using the leap-frog algorithm. The temperature was set by velocity-rescaling temperature coupling. Fast particle-mesh Ewald summation (PME) was used with a 6 nm real-space Coulomb cutoff, and a Fourier spacing equal to 0.6 nm to account for the long-ranged electrostatic contribution. For an in-depth description of the input parameters, the reader is referred to the user manual [21]. The box length used in the NVT simulations was 30 nm, corresponding to a volume fraction of 9% ($\phi \approx 0.09$). This value was chosen higher than the experimental samples due to the small size of the simulated platelets, where the average lateral size of a natural mmt platelet is approximately 250 nm [23]. The time step was set to 10 fs, with a total of 10^7 steps.

From the bulk MD simulations structural information were obtained via the total structure factor between the platelets, defined as:

$$S(q) = \left\langle \frac{1}{N}\sum_{i=1}^{N}\sum_{j=1}^{N}\frac{\sin(qr_{ij})}{qr_{ij}}\right\rangle, \tag{5}$$

where N is the total number of platelet sites in the system. Assuming an isotropic scattering, the equation of the total structure factor can be rewritten as:

$$S(q) = 1 + 4\pi\frac{N}{V}\int_0^{\infty}(g(r)-1)r^2\frac{\sin(qr)}{qr}dr, \tag{6}$$

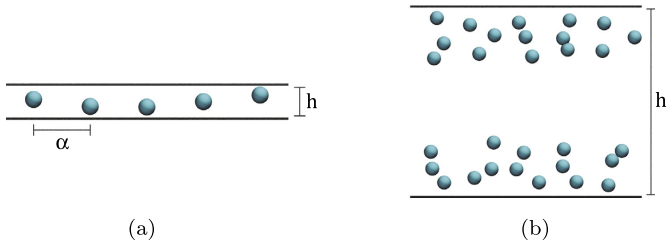

Fig. 1. Schematic illustration of two charged surfaces (represented as horizontal black lines) mediated by counterions (represented as cyan spheres). (a) The lateral distance, α, between the ions is larger than the separation, h, between the two charged surfaces. (b) The charged surfaces attract two separate layers of counterions, and the lateral distance between the ions is small.

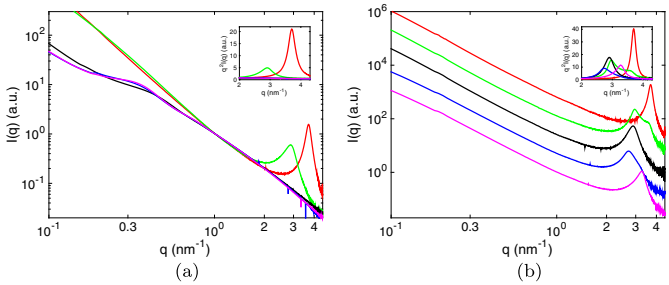

Fig. 2. The X-ray scattering intensities as a function of the scattering vector at T = 25 °C and $\phi_c \approx 0.06$ for (a) Na^+-, and (b) Ca^{2+}-montmorillonite at 95 (red), 60 (green), 40 (black), 20 (blue), and 0 (magenta) wt% EtOH. The insets show the Kratky plots of the corresponding systems. In (a) the scattering intensities are normalized at $q \approx 1$ nm^{-1}, and in (b) the scattering curves are scaled to enhance the different shape of the Bragg peaks. (For interpretation of the references to color in this figure legend, the reader is referred to the web version of this article.)

where $g(r)$ is the radial distribution function between all the platelet sites in the system. If $g(r)$ is not approaching one at large separations due to the finite length of the box, a window function can be used to reduce artefacts, according to:

$$S_w(q) = 1 + 4\pi\frac{N}{V}\int_0^\infty (g(r)-1)r^2\frac{\sin(qr)}{qr}\frac{\sin(\pi r/R_c)}{\pi r/R_c}dr, \quad (7)$$

where R_c is the maximum distance in $g(r)$ [24].

Two parallel infinite surfaces mimicking the clay platelets with corresponding counterions were simulated using Monte Carlo simulations. The model is described elsewhere [25]. The surfaces have a uniform surface charge density of $\sigma = -1.3$ e/nm^2, separated at a distance h. The counterions are treated as charged hard spheres, where the electrostatic interactions are defined similarly as for the bulk simulations. The system assumes equilibrium with salt-free water, and thus, the pressure is equal to the osmotic pressure. For a given temperature and separation between the surfaces, the osmotic pressure, $\Pi = \Pi(T,h)$, can be calculated using a midplane approach defined as: $\Pi = \Pi^{id} + \Pi^{corr} + \Pi^{coll}$, where $\Pi^{id} = k_BT\Sigma_{i=1}^{2}c_i(mp)$ is the ideal contribution, $c_i(mp)$ is the concentration of counterions at the midplane with valency i. Π^{corr} is an attractive term due to the ion-ion correlation interactions on either side of the midplane, and Π^{coll} is the collision term due to the finite ion size, where the diameter of an ion is $d_{hc} = 4$ Å [26].

For two equally charged surfaces the interactions in the system can be explained either with the weak or the strong coupling (SC) theory [27]. The Poisson-Boltzmann (PB) equation is asymptotically exact in the limit of weak coupling, i.e. long distances between the surfaces, low surface charge density, and low counterion valence. The SC theory is asymptotically exact in the opposite limit, i.e. short distances between the surfaces, high surface charge density, and high counterion valence. The limits can be found by considering the coupling parameter:

$$\Xi = 2\pi z^3 l_B^2 \sigma_s, \quad (8)$$

where σ_s is the surface charge number density. The SC theory is valid for $\Xi \to \infty$ (the SC limit), and the PB equation is valid for small values of Ξ. A schematic illustration of two charged surfaces mediated by counterions are shown in Fig. 1. The SC theory is valid if the lateral distance between the ions, α, is larger than the separation, h, between the surfaces, i.e. $h < \alpha$, see Fig. 1a, where the ions move independently of each other perpendicular to the surfaces due to the strong ion-ion correlation forces. The PB equation is valid in Fig. 1b, where each ion interacts with a diffuse cloud of other ions [27].

4. Results and discussion

4.1. SAXS

Scattering experiments were performed for different water/EtOH mixture conditions for Na-, and Ca-mmt, where the scattering intensities, and the Kratky plots ($q^2I(q)$ vs q), at T = 25 °C and $\phi_c \approx 0.06$, are shown in Fig. 2. Bragg peaks are clearly observed

Table 2
The position of the Bragg peak maximum (q_{max}), *d*-spacing (d_{Bragg}), full width at half maximum (FWHM), and average number of platelets per tactoid ($\langle N \rangle$), for Na^+-, and Ca^{2+}-montmorillonite.

wt% EtOH	q_{max} (nm^{-1})	d_{Bragg} (nm)	FWHM (nm^{-1})	$\langle N \rangle$
Na-mmt				
60	2.88	2.18	0.53	11
95	3.70	1.70	0.30	25
Ca-mmt				
0	3.25	1.93	0.38	17
20	2.77	2.27	0.54	10
40	2.90	2.17	0.40	15
95	3.69	1.70	0.20	37

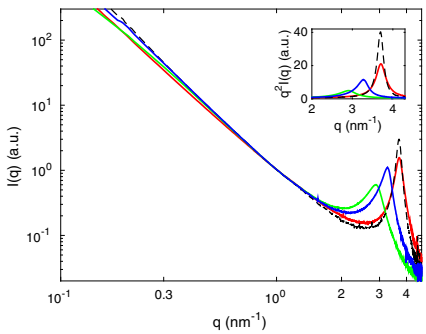

Fig. 3. The X-ray scattering intensities as a function of the scattering vector at T = 25 °C and $\phi_c \approx 0.06$ of Na^+-montmorillonite with 95 (red), and 60 (green) wt% EtOH, and Ca^{2+}-montmorillonite with 95 (dashed black), and 0 (blue) wt% EtOH. The inset shows the Kratky plots of the corresponding systems. The scattering intensities are normalized at $q \approx 1\ nm^{-1}$. (For interpretation of the references to color in this figure legend, the reader is referred to the web version of this article.)

for Na-mmt at water/EtOH mixtures above 60 wt% (Fig. 2a), indicating that tactoids are formed when increasing the concentration of EtOH, hence, it is possible to capture a crossover from a repulsive to an attractive system. As the concentration of EtOH increases from 60 to 95 wt% with respect to EtOH, the Bragg peak moves towards higher values of *q*, i.e. the separation between the platelets decreases from ~ 2.18 to 1.70 nm. Moreover, the full width at half maximum of the Bragg peaks decreases, indicating that the tactoids are growing in size, where the average number of platelets in the tactoids increases from $\langle N \rangle \sim 11$ to 25. For Ca-mmt (Fig. 2b) the position of the Bragg peak is strongly dependent on the EtOH concentration. When the concentration increases from 0 to 20 wt% EtOH, the separation between the platelets in the tactoids increases from ~ 1.93 to 2.27 nm. At 60 wt% EtOH the scattering pattern is a superposition of two Bragg peaks, indicating that there is a competition between two different separations, either of intercalated EtOH and water, or two EtOH concentrations. Above 60 wt% EtOH the separation between the platelets decreases, for example for 95 wt% EtOH it becomes ~ 1.70 nm. The values of the position of the Bragg peak, the *d*-spacing, the full width at half maximum, and the average number of platelets per tactoid for both Na-, and Ca-mmt, are shown in Table 2.

By comparing the scattering curves of Na-, and Ca-mmt with 95 and 0 wt% EtOH, respectively (Fig. 3), it is shown that the position of the Bragg peak of Na-mmt occurs at a higher q-value than Ca-mmt, i.e. ~ 3.70 and 3.25 nm^{-1}. This corresponds to a separation between the platelets in the tactoids of ~ 1.70 and 1.93 nm, respectively, indicating that there are stronger attractive interactions in the system with Na-mmt. The full width at half maximum is broader for Ca-mmt, resulting in a smaller average number of platelets in the tactoids c.f. $\langle N \rangle \sim 17$, while for Na-mmt $\langle N \rangle \sim 25$. Hence, by changing the solvent composition from water to EtOH, i.e. by decreasing the relative permittivity of the solvent, the structural properties of Na-mmt do indeed behave similarly as Ca-mmt.

Table 3
The coupling parameter as a function of EtOH concentration for Na^+-, and Ca^{2+}-montmorillonite.[a]

wt% EtOH	Ξ	d_{Bragg} (nm)	$\langle N \rangle$
Na-mmt			
0	3	–	–
95	28	1.70	25
Ca-mmt			
0	25	1.93	17
95	224	1.70	37

[a] The coupling parameter (Ξ), *d*-spacing (d_{Bragg}), and the average number of platelets in the tactoid ($\langle N \rangle$) for Na^+-, and Ca^{2+}-montmorillonite in 0, and 95 wt% EtOH, respectively.

The experimental results above can be qualitatively explained by comparing the coupling parameter, where $\Xi \sim 28$ for monovalent ions in 95 wt% EtOH, and $\Xi \sim 25$ for divalent ions in water at T = 20 °C, see Table 3. Thus, there are indeed stronger attractive interactions due to the stronger coupling with monovalent ions in EtOH compared to divalent ions in water. For divalent ions in 95 wt % EtOH, the coupling parameter is even higher, i.e. $\Xi \sim 224$. This effect is captured in the SAXS data, where the position of the Bragg peak is approximately the same for Na-, and Ca-mmt in 95 wt% EtOH, i.e. ~ 3.7 nm^{-1}. However, the FWHM of the peak is narrower for Ca-mmt corresponding to $\langle N \rangle \sim 37$, indicating that there are stronger attractive forces for the system with divalent counterions. Moreover, when monovalent counterions are replaced by divalent counterions, the number of ions decreases with a factor of two, which corresponds to a decreased double-layer repulsion.

The scattering intensities obtained from the temperature measurements of Na-, and Ca-mmt in 60, and 20 wt% EtOH, respectively, at T = 27, and 63 °C, with $\phi_c \approx 0.06$, are shown in Fig. 4. From the analysis of the Bragg peaks it is shown that there is only a minor deviation between the two temperatures for the two different systems, where the difference in separation between the temperatures, i.e. $\Delta d_{Bragg} = d_{Bragg}(T = 63\ °C) - d_{Bragg}(T = 27\ °C)$, were estimated to be ~ 0.01, and ~ 0.08 nm for Na-, and Ca-mmt, respectively, resulting in an average separation between the platelets in the tactoids of ~ 2.2 nm. Also, the FWHM is in the same order for all scattering curves, corresponding to an average number of platelets in the tactoids of ~ 10. From these measurements it can be concluded that there is only a minor temperature effect in the systems, in correlation to what has been noticed for Na-, and Ca-mmt in pure water [7].

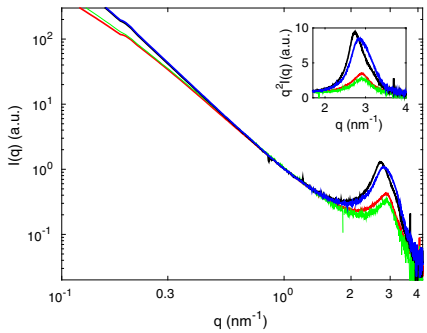

Fig. 4. The X-ray scattering intensities as a function of the scattering vector for the temperature measurements with $\phi_c \approx 0.06$ of Na^+-montmorillonite with 60 wt% EtOH at T = 27 (red), and 63 °C (green), and Ca^{2+}-montmorillonite with 20 wt% EtOH at T = 27 (black), and 63 °C (blue), respectively. The inset shows the Kratky plots for the corresponding systems. The scattering intensities are normalized at $q \approx 1$ nm^{-1}. (For interpretation of the references to color in this figure legend, the reader is referred to the web version of this article.)

4.2. Osmotic pressure

Fig. 5a shows the results from the osmotic pressure measurements of Ca-mmt at room temperature for two different values of the dry density: 1230, and 1180 kg/m^3. Each plateau corresponds to an equilibrium osmotic pressure of the clay system for the respective water/EtOH mixture in the order of 0, 20, 40, 60, 80, 95, and 0 wt% EtOH. By extracting the equilibrium osmotic pressures, it is clearly shown that there is a non-monotonic behavior of the osmotic pressure as a function of EtOH concentration, regardless of dry density (Fig. 5c), which correlates both with the SAXS data (Fig. 2b), as well as with the work done by Brindley et al. [11]. When the bulk solution is gradually changed from 0 to 95 wt% EtOH, the osmotic pressure increases at low concentrations, followed by a steady decrease at higher concentrations. The reversibility of the clay systems was confirmed by changing the solvent back to 0 wt% EtOH, where the osmotic pressure returns to its initial value. During this exchange, a large peak arises, which is enhanced in Fig. 5b. Our hypothesis is that the transition occurs via a successively replacement of intercalated EtOH molecules with water molecules, which is supported by analysing the height of the peak, where it is shown that the same magnitude is obtained at the highest recorded osmotic pressure. The same trend is also visible for the transition from 95 to 0 wt% EtOH for Na-mmt as for Ca-mmt, see Fig. 5b. The reader should notice, that the addition of 50 mM NaCl to the solution of 0 wt% EtOH with Na-mmt will not affect the measured osmotic pressure to a great extent, as shown in a previous publication [12]. The reason for this is due to the high volume fraction of the clay sample, where the counterion concentration is about one order of magnitude larger than the added salt concentration. For the same reason, with 95 wt% EtOH, the addition of 50 mM NaCl will only moderately increase the ion-ion correlation forces. However, the long-ranged repulsion is screened for more dilute samples [22]. The values of

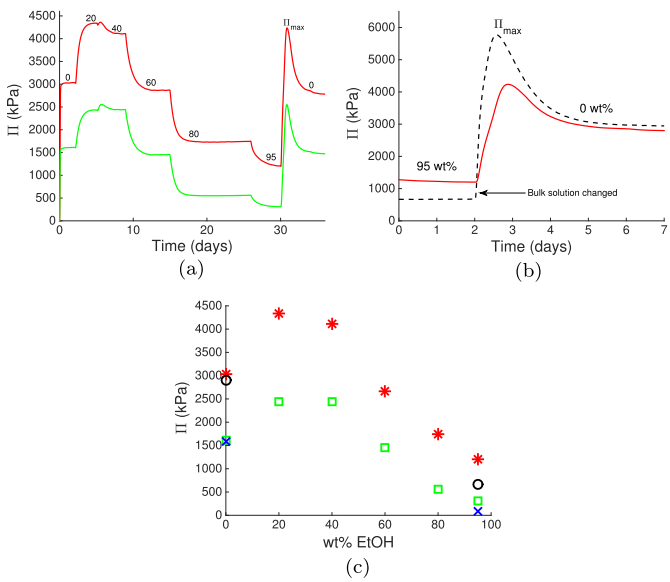

Fig. 5. (a) The osmotic pressure as a function of time and EtOH concentration of Ca^{2+}-montmorillonite at two different clay dry densities (D_d). (b) The transition from 95 to 0 wt% EtOH of both Na^+-, and Ca^{2+}-montmorillonite. (c) The equilibrium osmotic pressures of the respective EtOH concentrations for all systems. The color codes are: $D_d = 1230$ (red), and 1180 (green) kg/m^3 for Ca^{2+}-montmorillonite, and $D_d = 1070$ (black), and 1030 (blue) kg/m^3 for Na^+-montmorillonite. (For interpretation of the references to color in this figure legend, the reader is referred to the web version of this article.)

Table 4
The equilibrium osmotic pressures as a function of clay dry density for Na^+-, and Ca^{2+}-montmorillonite.[a]

D_d (kg/m^3)	Π_0 (kPa)	Π_{95} (kPa)	Π_{max} (kPa)
Na-mmt			
1070	2910	670	5770
1030	1590	90	2630
Ca-mmt			
1180	1610	310	2550
1230	3040	1210	4240

[a] The osmotic pressure of 0 (Π_0), and 95 (Π_{95}) wt% EtOH, and at the position of the peak maximum (Π_{max}) for Na^+-, and Ca^{2+}-montmorillonite, as a function of clay dry density (D_d).

the equilibrium osmotic pressures of 0 (Π_0), and 95 (Π_{95}) wt% EtOH, as well as the osmotic pressure at the position of the peak maximum (Π_{max}) for both Na-, and Ca-mmt, are given in Table 4.

4.3. Simulations

Radial distribution functions (rdfs) with respect to the center-of-mass between the platelets were extracted from the NVT MD bulk simulations at T = 20 °C, and with a volume fraction of 9% ($\phi \approx 0.09$). The number of peaks in the rdfs are an indication of the average number of platelets in the tactoids, $\langle N \rangle$, where the height of the peak gives the probability of finding that configuration. The first peak is equivalent to a structure when two platelets have aggregated face-to-face at a distance of ~ 1.3 nm, and the second peak corresponds to the situation where three platelets have aggregated at a distance of $\sim 1.3 \cdot 2$, and so on. As shown, both the number of peaks, and the probability of aggregation, increase with a decrease in the relative permittivity. When decreasing the relative permittivity of the solvent, the attractive ion-ion correlations are enhanced due to the increase in Bjerrum length, and thus an increase in the coupling parameter. This behavior is captured in the Na-mmt system (Fig. 6a), where peaks in the rdfs are found above 90 wt% EtOH. As expected, the simulated SAXS spectras (Fig. 6b) show Bragg peaks for 95, and 100 wt% EtOH, where the positions of the peaks are corresponding to a d-spacing of $\sim$1.2 nm for both systems. The discrepancy of the smoothness in the scattering pattern of the simulated SAXS spectra arises from the small size of the platelets. No Bragg peaks are observed at an EtOH concentration of 90 wt%, or lower, indicating the existence of a repulsive system. The transition from a repulsive to an attractive system is illustrated in Fig. 6c-d, where representative configurations of the Na-mmt system in 0, and 100 wt% EtOH, are shown. At 0 wt% EtOH, only single platelets are found in the system, whereas for 100 wt% EtOH, all platelets have aggregated and formed tactoids. In the latter, the average number of platelets per tactoid was determined to $\langle N \rangle \sim 4$. The MD simulations are in qualitative agreement with the SAXS data (Fig. 2a), where a transition from a repulsive to an attractive system is found for Na-mmt. In the simulations, the transition occurs at a higher EtOH concentration compared to the experimental data, which could arise from the selected input parameters, such as the volume fraction of the platelets, the surface charge density, and the size of the platelets.

By comparing the rdfs of Na-mmt at 95 wt% EtOH with Ca-mmt at 0 wt% EtOH (Fig. 7a), it is shown that the height of the first peaks are of the same magnitude, indicating that the probability of finding a face-to-face configuration is of the same order. For the Ca-mmt system, the second peak is more pronounced, indicating that larger aggregates have been formed. This is confirmed by comparing the representative configurations of the systems (Fig. 7c-d),

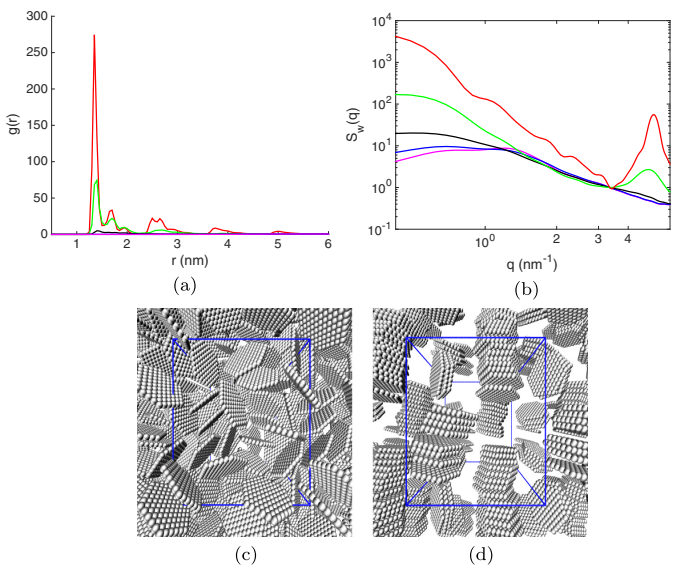

Fig. 6. (a) Radial distribution functions, and (b) simulated SAXS spectras from the NVT MD bulk simulations at T = 20 °C of Na^+-montmorillonite at 100 (red), 95 (green), 90 (black), 60 (blue), and 0 (magenta) wt% EtOH. Illustrative configurations of Na^+-montmorillonite at (c) 0, and (d) 100 wt% EtOH. The volume fraction of the system was 9% ($\phi \approx 0.09$). (For interpretation of the references to color in this figure legend, the reader is referred to the web version of this article.)

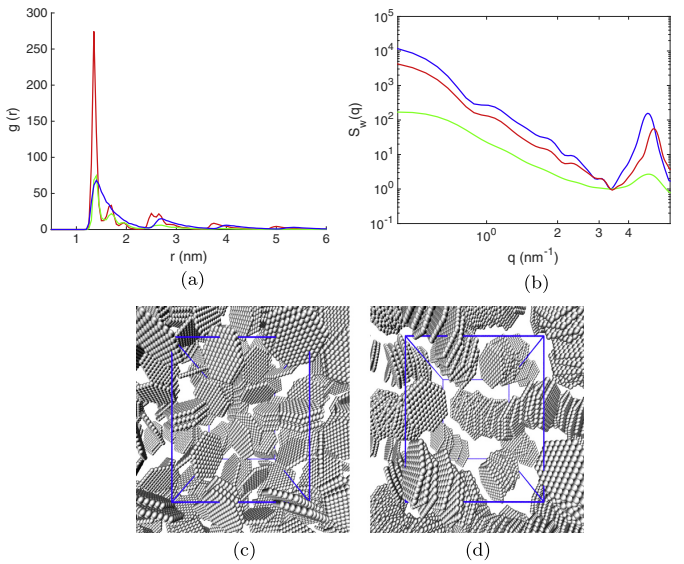

Fig. 7. (a) Radial distribution functions, and (b) simulated SAXS spectras from the NVT MD bulk simulations at T = 20 °C of Na^+-montmorillonite at 100 (red), and 95 (green) wt% EtOH, and Ca^{2+}-montmorillonite at 0 (blue) wt% EtOH. Illustrative configurations of (c) Na^+-montmorillonite at 95 wt% EtOH, and (d) Ca^{2+}-montmorillonite at 0 wt% EtOH. The volume fraction of the system was 9% ($\phi \approx 0.09$). (For interpretation of the references to color in this figure legend, the reader is referred to the web version of this article.)

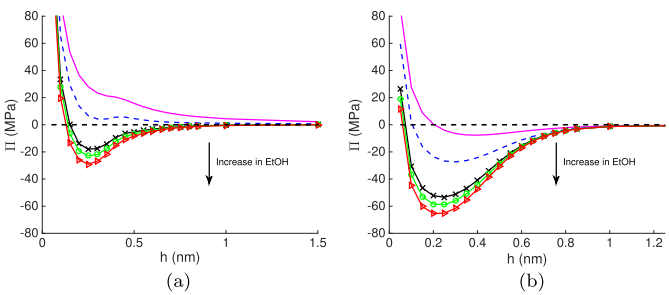

Fig. 8. The osmotic pressure as a function of separation between the surfaces from the MC simulations at T = 20 °C of (a) Na^+-, and (b) Ca^{2+}-montmorillonite at 100 (red), 95 (green), 90 (black), 60 (dashed blue), and 0 (magenta) wt% EtOH. The surface charge density was $\sigma = -1.3$ e/nm^2. (For interpretation of the references to color in this figure legend, the reader is referred to the web version of this article.)

where smaller tactoids are found for Na-mmt at 95 wt% EtOH compared to Ca-mmt at 0 wt% EtOH. Here the average number of platelets per tactoid becomes $\langle N \rangle \sim 2$, and 4 for each system, respectively. From the simulated SAXS spectras (Fig. 7b), the Bragg peak of the Ca-mmt system is shifted towards lower values of q compared to the Na-mmt system, which corresponds to a d-spacing of $\sim$ 1.3, and 1.2 nm, respectively. The MD simulations have a reasonable agreement with the SAXS data (Fig. 3), indicating slightly stronger attractive interactions in the Na-mmt system at 95 wt% EtOH, in comparison with the Ca-mmt system at 0 wt% EtOH.

The osmotic pressure as a function of separation between the surfaces from the MC simulations at T = 20 °C are shown in Fig. 8. For the Na-mmt system (Fig. 8a) both the osmotic pressure, and the equilibrium separation between the surfaces determined from $\Pi(h) = 0$ decrease with an increase in EtOH concentration. The transition from a repulsive to an attractive system occurs between 60, and 90 wt% EtOH, where a global minimum is found for the systems at 90 wt% EtOH and above. These results correlate with the SAXS data and the bulk MD simulations, indicating that the model also captures the behavior for Na-mmt in water/EtOH mixtures. This is, however, not the case for the Ca-mmt system

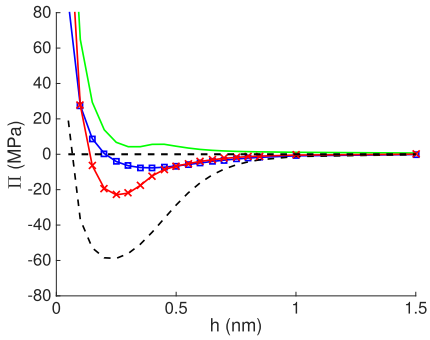

Fig. 9. The osmotic pressure as a function of separation between the surfaces from the MC simulations at T = 20 °C of Na^+-montmorillonite at 95 (red), and 60 (green) wt% EtOH, and Ca^{2+}-montmorillonite at 95 (dashed black), and 0 (blue) wt% EtOH. The surface charge density was $\sigma = -1.3$ e/nm^2. (For interpretation of the references to color in this figure legend, the reader is referred to the web version of this article.)

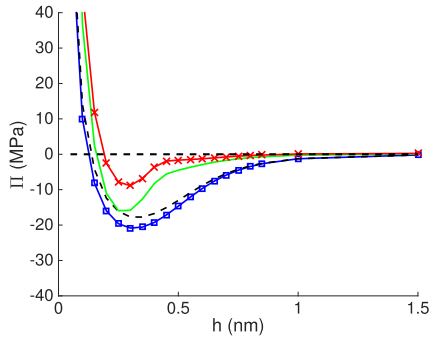

Fig. 10. The osmotic pressure as a function of separation between the surfaces for the MC simulations of Na^+-montmorillonite at 80 wt% EtOH, at T = 20 (red), and 60 °C (green), and Ca^{2+}-montmorillonite at 40 wt% EtOH, at T = 20 (black), and 60 °C (blue). The surface charge density was $\sigma = -1.3$ e/nm^2. (For interpretation of the references to color in this figure legend, the reader is referred to the web version of this article.)

(Fig. 8b), where the monotonic trend for the osmotic pressure as a function of EtOH concentration captured in the MC simulations, is not consistent with neither the SAXS nor the experimental osmotic pressure data. This non-monotonic behavior could not be captured utilizing the continuum model, probably due to the lack of partitioning of the solvent molecules. In principle, the continuum model should be valid with respect to the electrostatic interactions. However, the effect of the variation of the relative permittivity could be overruled by other effects, such as the difference in size between the solvent molecules, the density changes associated with the solvent interactions, as well as the geometry of the solvent molecules.

Comparisons between the osmotic pressure data obtained from the MC simulations for the Na-, and the Ca-mmt systems (Fig. 9), show the same trend as is found in the SAXS data. The attractive interaction forces are stronger, and the separation between the surfaces are smaller for Na-mmt at 95 wt% EtOH in comparison to Ca-mmt at 0 wt% EtOH. These results conclude that the model can accurately capture the behavior of the transition from a repulsive to an attractive system by tuning the electrostatic interactions, and confirm that the structural properties of Na-mmt do indeed behave similarly as a Ca-mmt when changing the solvent from water to EtOH.

The temperature effect has also been analyzed with the MC model. The simulated osmotic pressure of Na-, and Ca-mmt at two different temperatures are presented in Fig. 10. In order to capture the corresponding behavior as for the SAXS data (Fig. 4), a higher concentration of EtOH was chosen for both of the systems. An exact agreement is possible to find by tuning the fitting parameters. However, as for the MD bulk simulations, our goal with the model is to understand the physics behind the clay behavior, rather than obtaining correct fitting parameters. From these simulations it was found that there is only a minor temperature effect, where the attraction increases with an increase in temperature, resulting in a decrease in the separation between the surfaces. The separation differences between the two temperatures, i.e. $\Delta d_{Bragg} = d_{Bragg}(T = 60\ °C) - d_{Bragg}(T = 20\ °C)$, for Na-, and Ca-mmt were estimated to ~ 0.03, and ~ 0.01 nm respectively, and they are of the same order of magnitude as for the SAXS data.

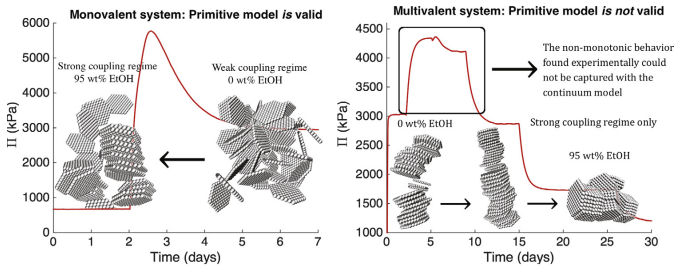

Fig. 11. (a) The osmotic pressure response of Na^+-montmorillonite, with illustrative configurations corresponding to 95 (left), and 0 (right) wt% EtOH. (b) The osmotic pressure response of Ca^{2+}-montmorillonite, where the black box represents the limitation regime of the continuum model, and the illustrative configurations correspond to 0 (left), 20 (middle), and 95 (right) wt% EtOH.

5. Conclusions

We have shown that it is possible to tune the electrostatic interactions to obtain a transition from a repulsive to an attractive system for Na-mmt via the solvent properties, i.e. by decreasing in the relative permittivity. From the SAXS data, Bragg peaks were found at 60, and 95 wt% EtOH, corresponding to a *d*-spacing of $\sim$ 2.18, and 1.70 nm, respectively. The Bragg peaks are an indication of tactoid formation, and the decrease in *d*-spacing concludes that the interaction between the platelets are dominated by attractive ion-ion correlation forces, which are enhanced as the concentration of EtOH increases. From the experimentally osmotic pressure measurements reversibility of the Na-mmt system was obtained. Our hypothesis is that the transition from 95 to 0 wt% EtOH occurs via a successively replacement of intercalated EtOH molecules with water molecules (future work). The results from the theoretical models are in qualitative agreement with the experimental data, giving a further indication of that the given models can explain the underlying physics in the system containing monovalent ions. This is illustrated in Fig. 11a, where the transition between weak and strong coupling regime is visible.

Moreover, a non-monotonic behavior of the intracrystalline swelling of Ca-mmt as a function of EtOH concentration was captured experimentally. It was found that the osmotic pressure increased until 20 wt% EtOH was reached in the sample, whereas the *d*-spacing obtained from SAXS in the 20 wt% EtOH sample increased in comparison with 0 wt% EtOH. Hence, this indicates that there are stronger repulsive forces in the Ca-mmt systems at lower concentrations of EtOH. At 60 wt% EtOH the scattering pattern from the SAXS data was found to be a superposition of two Bragg peaks, and the osmotic pressure is in same regime as at 0 wt% EtOH, indicating that there is a competition between two different separations, either for the intercalated EtOH and water, or for two EtOH concentrations. At 95 wt% EtOH the *d*-spacing was decreased to $\sim$ 1.70 nm, and the osmotic pressure was markedly reduced, due to the enhanced ion-ion correlation forces. The non-monotonic behavior found experimentally could not be captured utilizing the continuum model, probably due to the lack of partitioning of the solvent molecules. This is illustrated in Fig. 11b, where the limitation regime of the model is highlighted by the black box, i.e. the increase in osmotic pressure, and the representative configurations of the Ca-mmt systems at 0, 20, and 95 wt% EtOH, show that the separation between the platelets decreases with an increase in EtOH concentration. Thus, in the continuum model a monotonic behavior is found for the intracrystalline swelling of Ca-mmt as a function of EtOH concentration, where the enhanced attractive ion-ion correlation forces increase with a decrease in relative permittivity. To be able to capture this effect theoretically, a model considering the interactions between the solvent molecules and the clay platelets is needed. For example, a model where the solvent is treated explicitly is a good candidate.

Acknowledgement

Computational resources were provided by the Swedish National Infrastructure for Computing (SNIC) through LUNARC, the Center for Scientific and Technical Computing at Lund University. We acknowledge the European Synchrotron Radiation Facility (ESRF) in Grenoble, France, for providing beamtime, Dr. T. Narayanan and Dr. J. Möller, for providing assistance during measurements at ESRF. The pressure measurement facilities were kindly provided by Clay Technology AB in Lund, Sweden. The work was performed within the framework of the Swedish national strategic e-science research program eSSENCE.

References

[1] L. Guldbrand, B. Jönsson, H. Wennerström, P. Linse, Electrical double layer forces. A Monte Carlo study, J. Phys. Chem. 80 (1984) 2221–2228, https://doi.org/10.1063/1.446912.
[2] P. Mongondry, J.F. Tassin, T. Nicolai, Revised state diagram of Laponite dispersions, J. Colloid Interface Sci. 283 (2005) 397–405, https://doi.org/10.1016/j.jcis.2004.09.043.
[3] F. Pignon, A. Magnin, J.-M. Piau, B. Cabane, P. Lindner, O. Diat, Yield stress thixotropic clay suspension: investigations of structure by light, neutron, and X-ray scattering, Phys. Rev. E 56 (1997) 3281–3289.
[4] S. Cocard, J.F. Tassin, T. Nicolai, Dynamical mechanical properties of gelling colloidal disks, J. Rheol. 44 (2000) 585–594, https://doi.org/10.1122/1.551107.
[5] C. Martin, F. Pignon, A. Magnin, M. Meireles, V. Lelièvre, P. Lindner, B. Cabane, Osmotic compression and expansion of highly ordered clay dispersions, Langmuir 22 (2006) 4065–4075, https://doi.org/10.1021/la052605k.
[6] K. Norrish, The swelling of montmorillonite, Discuss. Faraday Soc. 18 (1954) 120–134, https://doi.org/10.1039/DF9541800120.
[7] A. Thuresson, M. Jansson, T.S. Plivelic, M. Skepö, Temperature response of charged colloidal particles by mixing counterions utilizing Ca/Na montmorillonite as model system, J. Phys. Chem. C 121 (2017) 7951–7958, https://doi.org/10.1021/acs.jpcc.7b00882.
[8] R.H. Dowdy, M.M. Mortland, Alcohol-water interactions on montmorillonite surfaces. I. Ethanol*, Clays Clay Miner. 15 (1967) 259–271, https://doi.org/10.1346/CCMN.1967.0150131.
[9] S. Metz, R.L. Anderson, D.L. Geatches, J.L. Suter, R. Lines, H.C. Greenwell, Understanding the swelling behavior of modified nanoclay filler particles in water and ethanol, J. Phys. Chem. C 119 (22) (2015) 12625–12642, https://doi.org/10.1021/jp512257z.
[10] G.W. Brindley, S. Ray, Complexes of Ca-montmorillonite with primary monohydric alcohols (clay-organic studies – VIII), Am. Mineral. 49 (1964) 106–115.
[11] G.W. Brindley, K. Wiewiora, A. Wiewiora, Intracrystalline swelling of montmorillonite in some water-organic mixtures (clay-organic studies. XVII), Am. Mineral. 54 (1969) 1635–1644.
[12] O. Karnland, S. Olsson, U. Nilsson, Mineralogy and Sealing Properties of Various Bentonite and Smectite-rich Clay Materials, SKB Technical Report TR-06-30, 2006, pp. 1–1.
[13] M. Segad, B. Jönsson, B. Cabane, Tactoid formation in montmorillonite, J. Phys. Chem. C 116 (48) (2012) 25425–25433, https://doi.org/10.1021/jp3094929.
[14] P. Van Vaerenbergh, J. Léonardon, M. Sztucki, P. Boesecke, J. Gorini, L. Claustre, F. Sever, J. Morse, T. Narayanan, An upgrade beamline for combined wide, small and ultra small-angle X-ray scattering at the ESRF, AIP Conf. Proc. 1741 (1) (2016) 030034. https://doi.org/10.1063/1.4952857.
[15] M. Sztucki, SAXS Utilities Download Page, 2011. <http://www.sztucki.de/SAXSutilities> (accessed Mar 2017).
[16] M. Segad, S. Hanski, U. Olsson, J. Ruokolainen, T. Åkesson, B. Jönsson, Microstructural and swelling properties of Ca and Na montmorillonite: (in situ) observations with cryo-TEM and SAXS, J. Phys. Chem. C 116 (13) (2012) 7596–7601, https://doi.org/10.1021/jp300531y.
[17] M. Segad, Microstructure determination of IQ-WB clays: a direct procedure by small-angle X-ray scattering, J. Appl. Cryst. 46 (2013) 1316–1322, https://doi.org/10.1107/S0021889813020931.
[18] M. Birgersson, O. Karnland, U. Nilsson, Freezing of Bentonite. Experimental Studies and Theoretical Considerations, SKB Technical Report TR-10-40, 2010, pp. 1–1.
[19] A. Thuresson, M. Ullner, M. Turesson, Interaction and aggregation of charged platelets in electrolyte solutions: a coarse-graining approach, J. Phys. Chem. B 118 (2014) 7405–7413, https://doi.org/10.1021/ja01350a001.
[20] G. Åkerlöf, Dielectric constants of some organic solvent-water mixtures at various temperatures, J. Am. Chem. Soc. 54 (11) (1932) 4125–4139, https://doi.org/10.1021/jp502015g.
[21] M. Abraham, van der Spoel, E. Lindahl, B. Hess, The GROMACS Developer Team, GROMACS User Manual, version 5.0.4, 2014.
[22] A. Thuresson, M. Ullner, T. Åkesson, C. Labbez, B. Jönsson, Monte Carlo simulations of parallel charged platelets as an approach to tactoid formation in clay, Langmuir 29 (2013) 9216–9223, https://doi.org/10.1021/la401272u.
[23] J.L. Michot, I. Bihannic, K. Porsch, S. Maddi, C. Baravian, J. Mougel, P. Levitz, Phase diagrams of Wyoming Na-montmorillonite clay. Influence of particle anisotropy, Langmuir 20 (2004) 10829–10837, https://doi.org/10.1021/la0489108.
[24] G. Gutiérrez, B. Johansson, Molecular dynamics study of structural properties of amorphous Al_2O_3, Phys. Rev. B 65 (2002) 104202, https://doi.org/10.1103/PhysRevB.65.104202.
[25] M. Segad, B. Jönsson, T. Åkesson, B. Cabane, Ca/Na montmorillonite: structure, forces and swelling properties, Langmuir 26 (2010) 5782–5790, https://doi.org/10.1021/la9036293.
[26] A. Thuresson, O. Karnland, B. Jönsson, Anomalous temperature behavior in clay swelling due to ion-ion correlations, EPL 114 (2016) 38002, https://doi.org/10.1209/0295-5075/114/38002.
[27] R. Netz, Electrostatistics of counter-ions at and between planar charged walls: from Poisson-Boltzmann to the strong-coupling theory, Eur. Phys. J. E 5 (2001) 557, https://doi.org/10.1007/s101890170039.

Printed by Media-Tryck, Lund 2019 NORDIC SWAN ECOLABEL 3041 0903

LUND UNIVERSITY

ISBN: 978-91-7422-648-5

Theoretical Chemistry
Department of Chemistry
Faculty of Science
Lund University

9 789174 226485